Influence of grinding operations on surface integrity and chloride induced stress corrosion cracking of stainless steels

NIAN ZHOU

Licentiate Thesis in Chemistry
KTH Royal Institute of Technology
School of Chemical Science and Engineering
Department of Chemistry
SE -100 44 Stockholm, Sweden

TRITA-CHE Report 2016:5
ISSN 1654-1081
ISBN 978-91-7595-838-5

Akademisk avhandling som med tillstånd av KTH i Stockholm framlägges till offentlig granskning för avläggande av teknisk licentiatexamen tisdagen den 25 februari kl 13:00 i sal Q34, KTH, Osquldasväg 6B (03 tr), 10044 Stockholm, Sweden.

Abstract

Stainless steels were developed in the early 20th century and are used where both the mechanical properties of steels and corrosion resistance are required. There is continuous research to allow stainless steel components to be produced in a more economical way and be used in more harsh environments. A necessary component in this effort is to correlate the service performance with the production processes.

The central theme of this thesis is the mechanical grinding process. This is commonly used for producing stainless steel components, and results in varied surface properties that will strongly affect their service life. The influence of grinding parameters including abrasive grit size, machine power and grinding lubricant were studied for 304L austenitic stainless steel (Paper II) and 2304 duplex stainless steel (Paper I). Surface integrity was proved to vary significantly with different grinding parameters. Abrasive grit size was found to have the largest influence. Surface defects (deep grooves, smearing, adhesive/cold welding chips and indentations), a highly deformed surface layer up to a few microns in thickness and the generation of high level tensile residual stresses in the surface layer along the grinding direction were observed as the main types of damage when grinding stainless steels. A large degree of residual stress anisotropy is interpreted as being due to mechanical effects dominating over thermal effects.

The effect of grinding on stress corrosion cracking behaviour of 304L austenitic stainless steel in a chloride environment was also investigated (Paper III). Depending on the surface conditions, the actual loading by four-point bend was found to deviate from the calculated value using the formula according to ASTM G39 by different amounts. Grinding-induced surface tensile residual stress was suggested as the main factor to cause micro-cracks initiation on the ground surfaces. Grinding along the loading direction was proved to increase the susceptibility to chloride-induced SCC, while grinding perpendicular to the loading direction improved SCC resistance.

The knowledge obtained from this work can provide a reference for choosing appropriate grinding parameters when fabricating stainless steel components; and can also be used to help understanding the failure mechanism of ground stainless steel components during service.

Keywords
stainless steel, surface integrity, residual stress, stress corrosion cracking, grinding

Sammanfattning

Rostfria stål utvecklades i början på 1900-talet och används där det finns krav på en kombination av mekaniska egenskaperna hos stål och god korrosionsresistens. Kontinuerlig forskning pågår för att möjliggöra mer ekonomisk produktion av rostfria komponenter och användning i mer krävande miljöer. En nödvändig del i detta arbete är att relatera komponenternas livslängd till produktionsprocessen.

Det centrala temat hos denna avhandling är den mekaniska slipprocessen. Slipning används ofta vid produktion av rostfria stålprodukter och ger varierande ytegenskaper som kraftigt påverkar komponentens livslängd. Inverkan av slipparametrar som kornstorlek, maskinkraft och användning av skärvätska har studerats för 304L austenitiskt rostfritt stål (Paper II) och 2304 duplext rostfritt stål (Paper I). Ytintegriteten påverkas i hög grad av slipparametrarna. Kornstorlek hos slipkornen visade sig ha störst inverkan. Ytdefekter (djupa spår, utsmetning, vidhäftande/kallsvetsade flisor och hack), ett kraftigt deformerat skikt upp till några mikrometer i tjocklek samt alstring av höga dragrestspänningar i ytan längs med slipriktningen observerades som de huvudsakliga skadetyperna. En hög nivå av anisotropa restspänningar indikerar att mekaniska effekter vid slipning dominerat över termiska effekter.

Slipningens inverkan på spänningskorrosionsbeteendet hos 304L austenitiskt rostfritt stål i en kloridmiljö har undersökts (Paper III). Ytans tillstånd påverkade den faktiska belastningen vid fyrpunktsböjprovning, som därmed avvek från de beräknade värdena enligt formeln i standarden ASTM G39. Dragrestspänningar från slipningen föreslogs vara den huvudsakliga orsaken till initiering av mikrosprickor på de slipade ytorna. Slipning längs med belastningsriktningen ökade känsligheten för kloridinducerad spänningskorrosion, medan slipning tvärs lastriktningen i hög grad förbättrade spänningskorrosionsmotståndet.

Kunskapen från detta arbete kan utgöra en referens för att välja lämpliga slipparametrar vid tillverkning av rostfria stålkomponenter och kan även användas för att förstå skadefall hos slipade rostfria stålkomponenter vid användning.

Nyckelord

rostfritt stål, ytintegritet, restspänning, spänningskorrosion, slipning

List of papers

This thesis is based on the following papers, which are referred to in the text by their Roman numerals.

I. N. Zhou, R. Lin Peng, R. Pettersson, Surface integrity of 2304 duplex stainless steel after different grinding operations, accepted by Journal of Materials Processing Technology.

II. N. Zhou, R. Lin Peng, R. Pettersson, Surface characterization of austenitic stainless 304L after different grinding operations, submitted to Journal of Materials Processing Technology.

III. N. Zhou, R. Pettersson, R. Lin Peng, M. Schönning, Effect of surface grinding on chloride induced SCC of 304L, submitted to Material Science and Engineering A.

The author's contribution to the papers:

I. The author's contributions to this article are the major part of the experiments, evaluation and writing, apart from some of the XRD measurements.

II. The author's contributions to this article are the major part of the experiments, evaluation and writing, apart from some of the XRD and thickness measurements.

III. The author's contributions to this article are the major part of the experiments, evaluation and writing, apart from some of the XRD measurements.

Acknowledgements

First of all, I would like to express my sincere gratitude to my main supervisor Rachel Pettersson and co-supervisor Ru Lin Peng. Thank you for the countless time that you have put into this project as well as support and encouragement all the way. Also, many thanks to Mikael Schönning and Timo Pittulainen at Outokumpu Stainless AB for all the support and valuable advice.

My colleagues at Högskolan Dalarna and Sandbacka Park, thank you all for creating a fun and enjoyable working environment. The experimental support from Ulf Modin is greatly appreciated.

Friends and family, this would not be possible without you. My deepest gratitude is to my husband Erik Hedman for his love and support.

This work was performed within the Swedish Steel Industry Graduate School with financial support from Outokumpu Stainless Research Foundation, Region Dalarna, Region Gävleborg, Länsstyrelsen Gävleborg, Jernkontoret, Sandviken kommun and Högskolan Dalarna. Special acknowledgements are to Staffan Hertzman and Stefan Jonsson for providing me the opportunity for the work.

Nian Zhou
Sandviken, January 2015

List of abbreviations

$\sigma_{\parallel}$	Residual stress parallel to the rolling/grinding direction
$\sigma_{\perp}$	Residual stress perpendicular to the rolling/grinding direction
σ^{γ}	Residual stress in austenitic phase
σ^{α}	Residual stress in ferritic phase
σ^{M}	Macro residual stress
$\sigma^{m,\gamma}$	Micro-residual stress in austenite
$\sigma^{m,\alpha}$	Micro-residual stress in ferrite
AD	As delivered
BCC	Body centered cubic, ferrite phase
BCT	Body centered tetragonal
BSE	Backscattered electron
Cl-SCC	Chloride induced stress corrosion cracking
ECCI	Electron channeling contrast imaging
FCC	Face centered cubic, austenite phase
FEG-SEM	Field emission gun scanning electron microscope
FWHM	Full Width at Half Maximum
PRE	Pitting resistance equivalent
R_a	Arithmetic average roughness
RD	Rolling direction
R_z	Average peak to valley height
SCC	Stress corrosion cracking
SE	Secondary electron
SEM	Scanning electron microscopy
TD	Transverse to rolling direction
XRD	X-ray diffraction

Contents

1. Introduction

1.1. Background

Stainless steel is a very successful man-made material. A major advantage of stainless steels is the high corrosion resistance, either at low or high temperatures, combined with good mechanical properties. Due to the diverse properties that can be achieved, stainless steels are extensively used in a variety of applications, such as general construction, chemical engineering, petrochemical and nuclear industries, food and beverage production. Unfortunately, the chloride ion, which exists in common environments like seawater, the kitchen or even in the human body, is found to make stainless steel prone to stress corrosion cracking (SCC). One review in 1983 showed that almost 37% of one thousand failures of austenitic stainless steel 304 in chemical industry were attributed to stress corrosion cracking [1], so the problem should be taken seriously. Combating SCC of stainless steels not only means the reduction of catastrophic failures, but also long-term cost savings and reduction of environmental impact.

It is well recognized that the surface geometrical, physical and mechanical properties of machined components have significant effects on their functional performance; service failures related to corrosion almost always initiate from the surface or subsurface. Depending on the applications, machining processes are nearly always needed for stainless steel components to obtain the required surface and dimensional accuracy. Grinding is an important and widely used surface finishing process, sometimes also used for bulk material removal. Grinding is a complex process with geometrically unspecified cutting edges [2]. The knowledge of the evolution of the surface and subsurface layers of stainless steels during grinding is very limited, in spite of the fact that the process can be critical to service failure.

1.2. Aim of this work

The current work is focused on surface integrity and stress corrosion cracking behaviour of stainless steel from the grinding operations. The aim of the first part (Paper I and Paper II) was to learn about the

interrelation between surface integrity in terms of surface roughness, surface defects, surface and subsurface microstructures, residual stresses and different grinding parameters. Abrasive grit size, machine power and grinding lubricant were identified as the most interesting parameters to be studied. The aim of the second part (Paper III) was to correlate the corrosion properties to the grinding operation, especially to determine the role of induced residual stresses and applied stress on the stress corrosion cracking behaviour. This study is relevant to industrial applications and contributes to the scientific understanding of SCC. The results obtained can provide a reference for choosing appropriate grinding parameters when fabricating stainless steel components; also to help understand the failure mechanisms during service

2. Stainless steels

2.1. Introduction

Stainless steels are iron-based alloys that contain a minimum of 10.5% chromium by mass [3]. Chromium reacts instantly with oxygen and moisture in the environment, therefore a protective oxide layer, known as the passive film, will be formed over the entire surface of the material [4]. This oxide layer is very thin, only 1-3 nanometers in thickness [5]; grows slowly with time and has self-healing ability. Chromium is the most significant alloying element affecting passivity, although other elements such as nickel, molybdenum and nitrogen can also be added to enhance the corrosion resistance and structural properties of stainless steels [6] [7] [8].

2.2. Categories

Traditionally, stainless steels are often categorized based on their microstructure. The most common structures are austenitic, ferritic, martensitic and duplex stainless steels.

2.2.1. Austenitic stainless steels

Austenitic stainless steels have a face centered cubic (FCC) crystal structure. They contain a minimum of 16% chromium, a maximum of 0.15% carbon and sufficient nickel and/or manganese to retain the austenitic structure [9]. Additional elements, such as molybdenum, copper, titanium or nitrogen can be added to modify properties for more critical applications. Austenitic stainless steels are non-magnetic and can only be hardened by cold working. This group of steels has lower thermal conductivity than other stainless steels or low-alloyed structural steels.

2.2.2. Ferritic stainless steels

Ferritic stainless steels, which have a body centered cubic (BCC) crystal structure, consist principally of iron and chromium. They contain very little carbon and no, or very little nickel. Compared with austenitic grades, they are ferromagnetic and generally have better engineering properties with higher thermal conductivity. Because of the reduced chromium and nickel content, they have lower corrosion resistance; however, the

resistance to stress corrosion cracking is higher than for some austenitic stainless steels [10].

2.2.3. Martensitic stainless steels

Martensitic stainless steels have a body centered tetragonal (BCT) crystal structure. They contain chromium and small additions of nickel, molybdenum and carbon [11]. They are usually hardened by quenching and tempered. Martensitic stainless steels are magnetic. The corrosion resistance is generally lower than the other members in the stainless steel family; they are often used for high hardness requirement. Martensite can also be formed as a result of deformation of metastable austenitic stainless steels.

2.2.4. Duplex stainless steels

Duplex stainless steels, containing relative high levels of chromium and a moderate amount of nickel, have a microstructure balanced to contain approximately equal proportions of the austenitic and ferritic phases [11]. Because of the duplex structure, they combine many of the beneficial aspects of both austenitic and ferritic stainless steels. They are ferromagnetic due to the ferrite content and the thermal expansion lies between that of the austenitic and ferritic stainless steels. Compared with austenitic grades, they provide excellent mechanical properties and improved corrosion resistance, especially resistance to stress corrosion cracking.

2.3. Machinability of stainless steels

The term machinability refers to the ease with which a metal can be machined to a desired shape with a satisfactory surface finishing at low cost [12]. Two main problems may be generated when machining components with poor machinability: short tool life and damaged surface [13] [14] [15] [16]. Austenitic and duplex stainless steels are difficult to machine compared to conventional steels or ferritic and martensitic stainless steels. Built-up edges formed on the cutting tool due to the high ductility and there is a tendency to rapid work hardening [17]. Low thermal conductivity leads to high machining temperature, which can burn the surface [18] or give high tensile residual stresses [19] in the machined surface. Transformation to martensitic can occur when machining austenitic stainless steels and significantly changes the

material properties [20]. Moreover, for duplex stainless steels, high ductility in combination with high strength makes chip breaking difficult, which deteriorates the surface finishing [21]. The quality of the machined surfaces plays a significant role in the performance of the component, such as fatigue life and resistance to stress corrosion cracking. Thus careful attention should be paid to surface properties when machining stainless steels, especially the austenitic and duplex grades.

3. Grinding

3.1. Grinding process

The grinding process employs abrasives that contain grains of hard mineral bonded in a matrix [2]. Grinding is a type of cutting, in which the cutting edges are randomly spaced and irregularly shaped. Figure 1 shows a sketch of how abrasive grains in a grinding wheel remove material from a workpiece. During grinding, each grain acts as a microscopic single-point cutting edge and shears a short chip with gradually increasing thickness. Because of the irregular shape of the grains, sometimes ploughing occurs between the grain and the workpiece instead of cutting [22].

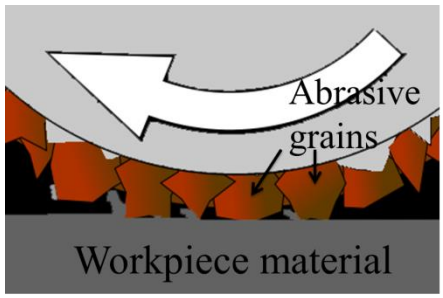

Figure 1 Schematic drawing of a grinding wheel, showing abrasive grains remove material from a workpiece.

Grinding is often categorized as a separate process from the conventional cutting processes (turning, milling, drilling, etc.). There are several aspects make it different from the other metal removal processes, these differences are mainly due to the difference in nature of cutting tools in grinding. In most cutting processes, the cutting tools have positive rake angles. However in the grinding process, a large variety of grain shape results in large negative rake angles [2]. The cutting depth of each grain is very small (a few μm) which results in the formation of very small chips; these chips easily adhere to the workpiece or abrasive surfaces [21]. The specific cutting energy for grinding is very high and more than 70 percent of the energy goes into the ground surface [23]; this increases the surface temperature and generates considerable tensile residual stresses [24].

Grinding fluid is sometimes used to cool the material and abrasives, to reduce the interface friction between the workpiece and the abrasive grains, and to remove the chips and reduce adhesion of chips. The choice of lubricant depends largely on the workpiece material [2].

3.2. Residual stresses in grinding

During grinding, mechanical and thermal actions between the workpiece material and the abrasive grains happen simultaneously. As illustrated in Figure 2, the sources for these actions mainly include five parts: deformation from shearing zone, friction from rake face, cutting-off work from cutting edge, friction from the flank and friction from bonding.

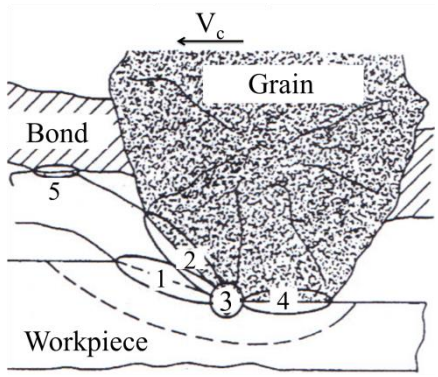

Figure 2 Sources of mechanical and thermal actions in grinding: (1) deformation from shearing zone, (2) friction from rake face, (3) cutting-off work from cutting edge, (4) friction from flank, (5) friction from bond; modified from [25].

The residual stress in grinding is governed by the complex coupling of both mechanical and thermal actions; the relative significance of these two factors varies from one process to another [24] [26]. Depending on the plastic deformation mode, tension or compression, mechanically induced residual stresses can be either tensile or compressive. In the grinding direction, the surface layer experiences overall compressive plastic deformation, the constraint by the subsurface results in tensile residual stresses in the surface layer [27]. In the transverse direction, tensile deformation is dominant. Surface compressive stresses are generated due to the interaction between the surface layer and the bulk [28]. However, thermally induced residual stresses are usually tensile. Thermal actions generate heat in the surface layer, thus a temperature

gradient is formed from surface to the bulk. After the grinding zone moves away, contraction of the surface layer will be hindered by the low temperature bulk, thus tensile residual stresses are generated in both directions during the cooling period [25] [29]. Other thermal impacts such as phase transformation or dynamic recrystallization can also induce residual stresses due to structure alteration and volume change of the surface layer material [28]. The size and depth of residual stresses induced by both mechanical and thermal actions depend largely on the cutting and frictional conditions between the abrasive and the workpiece material [30].

3.3. Published work on grinding

Grinding has great importance in the steel industry. It is widely used as surface finishing process to get the precise dimension of the component, although sometimes it is also used as bulk removal. The performance of grinding has been proved to be largely influenced by the settings of the operation, such as abrasive grit material [24], workpiece material [21], abrasive grit size [31], abrasive grain shape [32] and grain rake angle [22], grinding depth [24], grinding speed [22], feed rate [28], grinding lubricant [33] and etc. However, compared with other machining process, relatively little work has been published on grinding, especially in grinding stainless steels with well controlled grinding parameters.

4. Surface integrity

A good understanding of the changes in the surface layer is required to improve the product quality. Typical surface alternations include topological (geometric), metallurgical, mechanical, chemical and other changes [34]. The concept of surface integrity was first introduced in a technical sense by Field and Kahles [35]; they defined it as the 'inherent or enhanced condition of a surface produced by machining processes or other surface generation operations'. Their subsequent comprehensive review of surface integrity issues of various alloys from machining processes is among the first published literature on this topic, and this work emphasized the metallurgical alterations [36]. They later also provided a detailed description of measuring methods available for surface integrity inspection as well as an experimental procedure for assessing surface integrity parameters [37]. Their pioneering work made a significant contribution to the subject, which led to the subsequent establishment of an American National Standard on Surface Integrity [38]. In modern manufacturing processes, special knowledge and analysis of surface integrity can effectively assist in optimization and adaptive control, give a good compromise between the function of the surface and the minimization of production time and cost.

4.1. Surface roughness

Surface roughness is the foremost characteristic of surface integrity issues caused by machining tools used in the process. Roughness is the primary indicator related to the machinability of the workpiece material, the machining conditions, the tool form, the tolerance requirements and the tribological phenomena of the technological surfaces [25]. Furthermore, achieving a desired surface roughness is also critical in determining the service performance of the machined component. Reduced stress corrosion cracking resistance of X70 gas pipelines was observed with increased surface roughness [39]. Micro-notches induced by machining will generate a localized plastic strain field when a stress is applied, due to stress concentration at the notch tip; so fatigue cracks and stress corrosion cracks are prone to initiate in this zone of plasticity [40] [41]. Fatigue micro-cracks have been suggested to initiate from persistent slip bands or grain boundaries instead of the surface of machined specimens with low surface roughness [42]. The effect of surface roughness on the

component's life performance can also be correlated to other factors. Stress corrosion crack concentration has been reported to increase with increasing surface roughness, which may be related to the concentration of surface damage and hence potential initiation sites for cracks to nucleate [39]. Due to the higher tensile residual stresses combined with applied stress, pitting has been reported to be most significant on the ground surface despite a much low Ra value compared to the milled samples [19]. When machining stainless steels, surface roughness of the workpiece material is largely affected by the machining method and the parameters used [43] [44] [45].

4.2. Surface defects

Different forms of defects can be left on the surface after the machining process. Waviness, grooves, smearing, chip re-deposition, feed marks, cavities and cracks are the ones most often observed on the machined surfaces [25]. Problems can be caused from the surface defects during the service. A greater propensity for pitting has been reported at local defect sites on the machined surfaces [19] [46], and these pits were found to act as precursors to cracks. Failure at small grinding defects has been observed as predominant failure mode of a clean spring steel in the very high cycle fatigue regime [47]. A complete elimination of surface defects of a machined component is not possible; but based on the properties of the material, these defects can be reduced by choosing the proper machining parameters [48].

4.3. Microstructural alterations

The main surface damage of a machined component comes from mechanical loading and thermal impact which occur simultaneously during the machining operations. Both are all strongly influenced by the machining parameters. Microstructural alterations of the machined surfaces, such as deformation hardening [34], phase transformation [20], grain fragmentation [49], white layer formation [50], grain recrystallization [51], are result from these effects. The properties of the machined components are closely related to the microstructure of the surface layer. An increased hardness of the surface has been reported, and a work hardened surface layer can increase the difficulty for the subsequent cutting of materials with high work hardening rate [52]. The presence of strain induced martensite on the surface from machining has

been shown to increase the SCC susceptibility of 304L austenitic stainless [49]. The improvement of stress corrosion cracking resistance by grain refinement from laser peening of 304 austenitic stainless steel has been demonstrated [53]. The white layer is normally hard and brittle, cracks were found to easily nucleate and propagate in the surface white layer [54].

4.4. Residual stresses

Residual stresses are stresses that remain in the material after the original cause has been removed; they can arise in almost every step of processing [27]. Although residual stresses can have different origins such as mechanical, thermal or metallurgical causes, they are all the results of misfit; these misfits can be between different regions, different parts, or different phases [55]. Residual stresses may be desirable or undesirable. Depending on the workpiece material and the machining processes, both tensile and compressive residual stresses with varied magnitude can be generated in the surface and subsurface layers of the component [56] [57]. Surface compressive residual stresses are generally considered to be beneficial for the life performance of a component; while surface tensile residual stresses should be avoided. Multiple and interacting cracks have been reported on the milled surface of AISI 316 after exposure in boiling magnesium chloride for two weeks without applying any external load; the main driving force for the crack formation has been demonstrated to be the surface tensile residual stresses from the milling operations [58]. The compress residual stresses from massive laser peening of AISI 304 have been shown to have a beneficial effect on the stress corrosion cracking resistance [53]. Another problem that can be caused by the residual stresses is the dimensional instability; a change in dimension with time of a machined component may cause problems in structural assembling [59].

5. Corrosion of stainless steels

If the environment is too harsh, stainless steels can suffer from several types of corrosion, such as uniform corrosion, crevice corrosion, pitting, stress corrosion cracking, intergranular corrosion, galvanic corrosion and corrosion fatigue [10]. Below, two types of corrosion that are relevant to this work are discussed.

5.1. Pitting corrosion

Pitting corrosion is a localized form of attack at small discrete areas. Pits can look quite small at the surface and be hidden by apparently inoffensive corrosion products, but they may have larger area beneath the surface; thus pitting can remain undiscovered until failure [10]. Pitting results from a failure of the passive layer and the mechanisms of this pit initiation have been widely discussed but still not fully understood. The main mechanisms proposed are the penetration mechanism, the film-breaking mechanism and the adsorption mechanism [60]. The penetration mechanism involves the transport of anions through the oxide film to the metal surface where they start specific actions. For the film-breaking mechanism, rupture of the passive film gives direct access of the anions to the bare metal surface. The absorption mechanism begins with the adsorption of aggressive anions at the oxide surface, thus the metal cations from the oxide are catalytically enhanced to transfer to the electrolyte, leading to the thinning of passive film until total removal.

In contrast, the propagation of pitting is relatively well understood. Once the pit nucleates, the unprotected metal becomes anode and the surrounding environment acts as cathode, so a galvanic cell is formed. If no repassivation takes place, the large cathode-to-anode surface ratio will result in rapid local corrosion [10]. As the pit continues to grow, the pH value in the pit will decrease due to the hydrolysis of dissolved metal ions; this in turn further concentrates anions such as chloride ions in the pit [4]; the environment inside the growing pit becomes more aggressive and repassivation becomes even less likely, thus pits often propagate at a high rate. The mechanisms for pit initiation and propagation are illustrated in Figure 3.

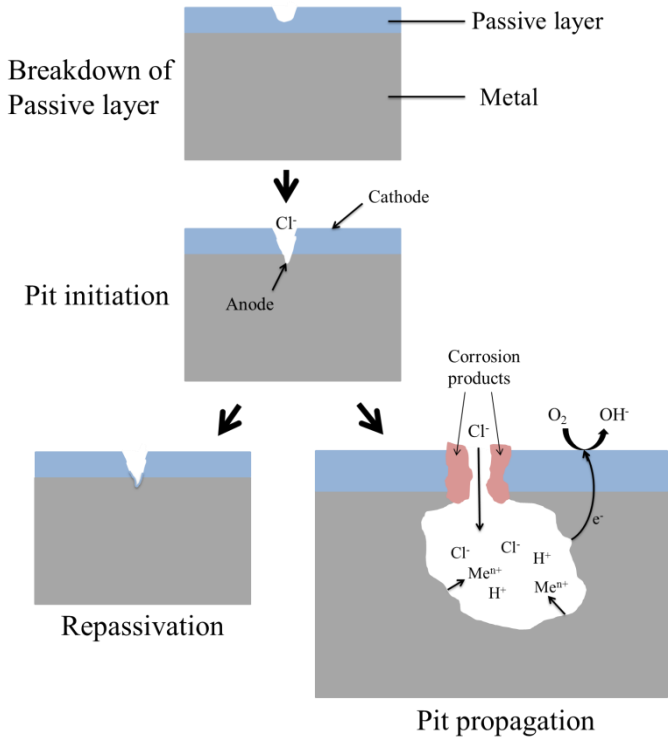

Figure 3 Schematic drawing of the pit initiation and propagation mechanisms.

For stainless steels, the pitting resistance equivalent (PRE) is often used as an index for ranking resistance to pitting corrosion. In general, the higher the PRE value, the better the resistance to pitting. "Super" is often used as a descriptor for an alloy with PRE value above 40, such as superaustenitic or superduplex stainless steels. PRE is calculated from the chemical compositions of stainless steels [10]:

$$\mathrm{PRE} = \%\mathrm{Cr} + 3.3 \times \%\mathrm{Mo} + 16 \times \%\mathrm{N} \qquad 5.1$$

5.2. Stress corrosion cracking

Stress corrosion cracking (SCC) is a brittle failure caused by the interaction of three factors: a susceptible alloy, a corrosive environment and the presence of sufficient tensile stresses (Figure 4) [4]. Cracks may be transgranular or intergranular depending on the microstructure of the material and the nature of the environment [4]. Due to the high

propagation rate, sudden failures caused by stress corrosion cracking often happen without warning.

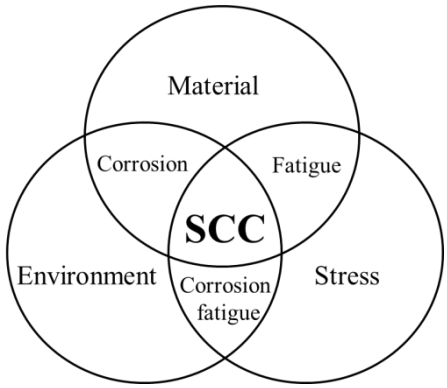

Figure 4 Simultaneous susceptible material, critical corrosive environment and threshold tensile stress required for stress corrosion cracking.

Many different models have been proposed to explain the mechanism of stress corrosion cracking [60]. Normally, a threshold stress is required to initiate SCC; depending on the metal and environment, the stress values varies a lot. In some cases, relatively low loading or even tensile residual stresses left from the manufacturing process may provoke stress corrosion cracking [58]. However, if compressive stresses are introduced, the resistance to stress corrosion cracking will be increased. Compressive stresses in the surface can delay crack initiation, and at depth can slow down the growth of cracks from the surface [53]. Stress corrosion cracking may also nucleate from other types of localized corrosion. Stress concentration and the acidity required for cracking can be achieved from some areas of pitting, intergranular corrosion or crevice corrosion [60].

For stainless steels, the most frequent attack which results in stress corrosion cracking is from chlorides. The risk of SCC increases with increasing temperature, increasing concentration of chloride and decreasing pH value of the environment [10]. Standard austenitic stainless steels are among the most sensitive group of stainless steels to chloride-induced stress corrosion cracking, while high-alloyed austenitic stainless steels may show good cracking resistance. Ferritic stainless steels generally have higher resistance to Cl-SCC; however, they are less resistant to pitting and crevice corrosion and are usually more sensitive to

hydrogen-related cracking. Duplex stainless steels with a combination microstructure of austenite and ferrite have much better Cl-SCC resistance than that of the classic austenitic grades [61].

There are different ways to evaluate the stress corrosion cracking susceptibility of stainless steels. There are a number of standardized testing environments, including boiling ~45% (by weight) aqueous magnesium chloride solution at 155.0 ± 1.0℃ according to ASTM G36 [62] and boiling 25% (by mass) sodium chloride acidified to pH 1.5 at ~108℃ standardized in ASTM G123 [63]. In addition, SCC tests can be done under constant strain or constant load conditions described by ISO and ASTM standards. Bent-beam [64], U-bend [65], C-ring [66], slow strain rate [67] are all widely used. The method chosen is critical to the outcome of the test; since corrosion behaviour can vary a great deal with different testing conditions [61] [68].

6. Experimental work

6.1. Materials

Two grades of stainless steels, austenitic 304L and duplex 2304, have been used in the current work. The austenitic grade is very widely used for many applications, while duplex stainless steels are newer alternatives with the attractive property of higher strength. The materials were industrially produced in Outokumpu Stainless AB, and they were delivered in the form of test coupons with dimensions 400mm×150mm×2mm. The as-delivered materials had been solution annealed (1100℃, forced air and water quenched), thereafter pickled and roll leveled. EBSD mapping showing the microstructure of the two materials are presented in Figure 5. The chemical compositions in wt% and the mechanical properties measured perpendicular to the rolling direction at room temperature are given in Table 1 and Table 2, respectively. Both duplex stainless steel 2304 (Paper I) and austenitic stainless steel 304L (Paper II) were used for surface integrity studies. For the corrosion studies (Paper III), the austenitic 304L stainless steel was used.

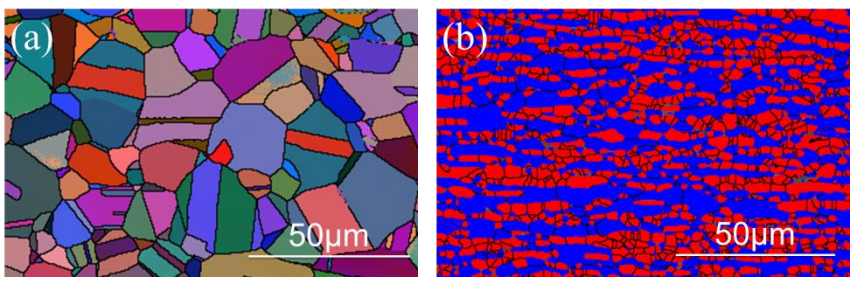

Figure 5 Cross-section microstructure of: (a) 304L austenitic stainless steel showing grain orientation, (b) 2304 duplex stainless steel showing red austenitic phase and blue ferritic phase.

Table 1 Chemical composition (wt%, Fe-balance) of the stainless steels investigated.

Grade	In paper	C	Si	Mn	P	S	Cr	Ni	Mo	Nb	N	Cu	Co	Ti
2304	I	0.019	0.39	1.48	0.028	0.001	23.35	4.84	0.36	-	0.125	0.22	-	0.006
304L	II, III	0.019	0.32	1.55	0.029	0.001	18.22	8.11	-	0.011	0.071	0.31	0.16	-

Table 2 Mechanical properties of the stainless steels measured perpendicular to the rolling direction at room temperature.

Grade	In paper	$R_{po.2}$(MPa)	R_m(MPa)	Elongation (%)	Hardness (HB)
2304	I	590	739	30	228
304L	II, III	230	642	54	170

6.2. Grinding operations

The grinding operations were conducted on a Chevalier FSG-2A618 grinding machine; the set-up is shown in Figure 6. A Kemper RADIX Go grinding wheel (50mm in width, 150mm in diameter), which is an expanding roller made of 20mm thick rubber, was used. During grinding, grinding belts (50mm in width, 473mm in length) with conventional aluminum oxide grit were mounted on the grinding wheel and test coupons (400mm×150mm×2mm) were mounted on the working table. A fixed grinding speed $v_s = 23$m/s and a fixed feed rate $v_w = 8$m/s were used. All grinding operations were performed along the rolling direction of the workpiece material.

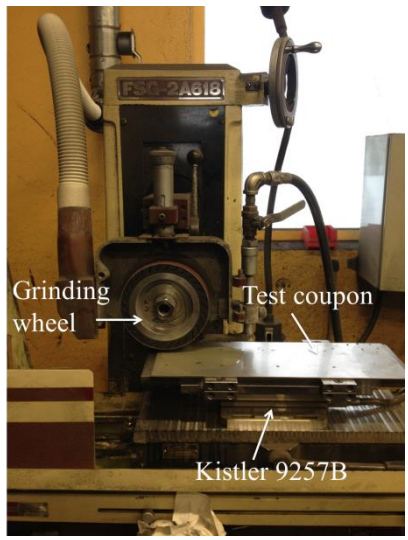

Figure 6 The grinding set-up.

Both duplex 2304 and austenitic 304L stainless steels were ground; an overview of the grinding parameters used is given in Table 3. Grinding parameters that were varied were abrasive grit size, machine power and

grinding lubricant. The machine power denotes the percentage of the total motor power to drive the grinding belt around; the total motor effect is 1kW. A piezo-electric transducer based dynamometer Kistler 9257B (Figure 6) was mounted under the working table to measure the normal force acting on the contact zone between the abrasive and workpiece material. During grinding, the grinding force was varied by changing the machine power; a given machine power was set and the induced normal grinding force was measured. The grinding lubricant used was Mobilcut 321 of 3% concentration; it is a synthetic fluid with a pH value of 9.4 and specific gravity of 1.10 at 20℃. The cooling system of the grinding machine was cleaned before grinding operations and new lubricant was used from beginning. During grinding operations, the used lubricant flowed into a chamber where large chips and particles sink down to the bottom. The fluid then flowed into a smaller chamber and was pumped up onto the workpiece surface again. Surface integrity has been investigated for all the specimens ground with different parameters, including both duplex 2304 (paper I) and austenitic 304L (paper II) stainless steels. For the corrosion studies (paper III), only austenitic 304L grade ground with 60# final surface finish, 60% machine power and without grinding lubricant was used.

Table 3 Overall view of the grinding parameters.

Group No.	Comparison	Final surface finish	Machine power	Lubricant	In paper
i	Abrasive grit size	60#	60%	without	I/II, III
		180#			I/II
		400#			
ii	Machine power	180#	30%	without	
			60%		
			90%		
iii	Lubrication	180#	60%	without	
				with	

An infrared camera FLIR i5 was used to measure the surface temperature of the workpiece during grinding; the measuring spots were near the contact area between the grinding wheel and the workpiece material. The emissivity setting of the camera was 0.95 both with and without lubricant. Since temperature measurements are strongly influenced by the surface conditions and the camera settings, the measured results in this study only provided an indication of the trends in temperature change with different grinding parameters.

6.3. Corrosion studies

The purpose of the corrosion tests (paper III) was to determine the influence of surface grinding on the SCC behaviour. The 304L austenitic stainless steel ground with 60# final surface finish, 60% machine power and without grinding lubricant was used. Three types of specimens were corrosion tested. All specimens were water jet cut from the test coupons. As illustrated in Figure 7, the specimens cut with the long axis parallel to the rolling/grinding direction, are denoted ground-RD and transverse to rolling/grinding direction, are denoted ground-TD. The as-delivered specimens cut parallel to the rolling direction, denoted AD, were tested as reference.

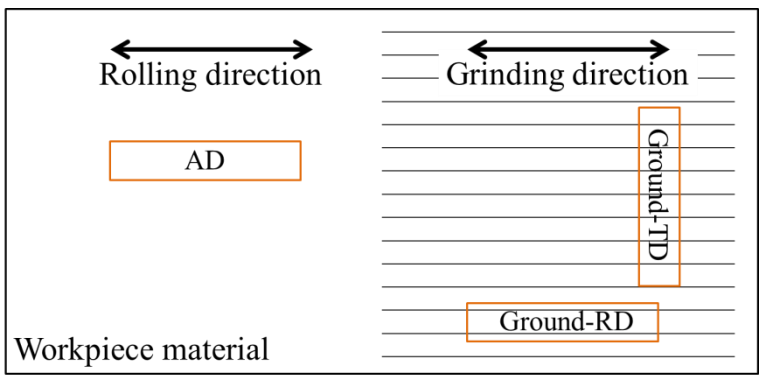

Figure 7 Schematic illustration of the orientation and designation of the specimens for corrosion tests.

Boiling magnesium chloride solution according to ASTM G36 [62] was used as the test environment. The specimens were exposed in a flask connected to a water cooled condenser and a thermometer; solution temperature was carefully maintained at 155 ± 1°C. Before exposure, all

the specimen edges were ground down using 800# abrasive paper to avoid sharp edges. Specimens were then allowed to passivate in air for at least 24 hours.

The susceptibility to chloride induced stress corrosion cracking was tested in two ways. The first set of tests was without applying external loading to investigate the role of residual stresses. All three types of specimens (dimension 45mm×10mm×2mm) were exposed. After 20 hours, the specimens were removed and checked for macro-cracks using a stereo microscope. If no macro-cracks were observed, the specimens were then put back for another 20h exposure. In the second series of tests, four-point bend loading (dimension 65mm×10mm×2mm) to different levels was applied according to ASTM G39 [64]. The loading direction was along the longitudinal direction. After application of the load, specimens were kept one hour in air to allow possible stress relaxation before exposure. In this case, the exposure period was 24 hours.

6.4. Characterization techniques

6.4.1. 3D optical surface profilometry

To get a first impression of the ground surface topography, a Wyko NT 9100 3D optical surface profilometer has been used in the current work. These measurements result in both 2D and 3D pictures of the surface morphology as well as some mathematical parameters describing the surface. This method is rather quick and has a depth resolution of 5nm. However, the samples have to reflect light; otherwise coating deposition is required.

From each area (1.3 mm×0.95 mm) of measurement, roughness values, both R_a and R_z, are calculated. The R_a value is an arithmetic average roughness, i.e. the arithmetic average value of roughness profile determined from deviations about the mean line over the evaluation length [25]. The R_z value is the average peak to valley height [25]; here it is the difference between the mean value of the five maximum peak heights and the five minimum valley depths from an arbitrarily chosen reference line over the measured surface. In the current work, five areas of each ground samples were measured, and the roughness is the average of these five measurements.

6.4.2. Stereo microscope

A Nikon SMZ-2T stereo microscope with ColorView Soft camera and Cell^A ColorView Soft image software of ×10-63 magnification was used to check the presence of macro-cracks in the specimens after exposure. The stereo microscope is an optical microscope and uses light reflected from the sample surface rather than transmitted through it [69]. It can provide a 3D visualization of the examined sample. This technique has rather poor depth resolution but is fast and gives valuable information, such as whether macro-cracks have been formed and where they are, for more detailed investigations.

6.4.3. Scanning electron microscopy

The possibility to characterize morphology and microstructure with good resolution at high magnification is of great importance in studies of the surface integrity and corrosion behaviour. In this work it was made by using scanning electron microscopy (SEM). By accelerating an electron beam onto the sample, signals containing different information about the material investigated can be generated. The electrons in the beam are emitted from an electron source, which in the instruments used for the current work is the field emission gun. Each signal comes from particular interactions between the atoms at/near the sample surface and the incident electrons. The signals used for this study include secondary electrons (SE) and backscatter electrons (BSE).

The most common imaging mode uses secondary electrons. SEs are the ejected electrons from atoms due to the inelastic scattering interactions between the primary electrons and the valence electrons of the sample atoms [70]. Generally, all electrons emitted from the specimen with an energy less than 50eV are considered as secondary electrons [71]. Because of the low energy of these electrons, only those produced near the surface of the sample are able to exit and be collected by the detector. The production of SEs is very dependent on the surface morphology. The SEs can produce very high resolution images of the sample surface; the surface sensitivity, signal intensity and resolution can be optimized by changing the beam current, the working voltage or apertures.

Backscattered electrons are from the primary incident beam that is ejected back out from the sample; they are used to produce a different

kind of image. Compared with SEs, BSEs have higher energy (> 50eV); therefore they have larger escape depth. So the information they produce is less restricted to the surface details; however this also results in reduced resolution. The electron channeling phenomenon was first discovered by Coates; he found a strong variation in backscattered electron emission as a function of the relative orientation between the incident electron beam and the crystal lattice (Figure 8) [72]. Directly after that, Booker et al. explained Coates's observation on a theoretical basis. They noted that for particular orientations, the BSEs intensity changes sharply; these critical beam-crystal orientations are those which satisfy the Bragg condition for a given set of lattice planes [73]. They also outlined the general framework of using electron channeling phenomenon for dislocations. Now electron channeling contrast imaging (ECCI) has been successfully used to capture local change in crystal orientation, deformation, strain field or even individual defects in crystalline materials [74].

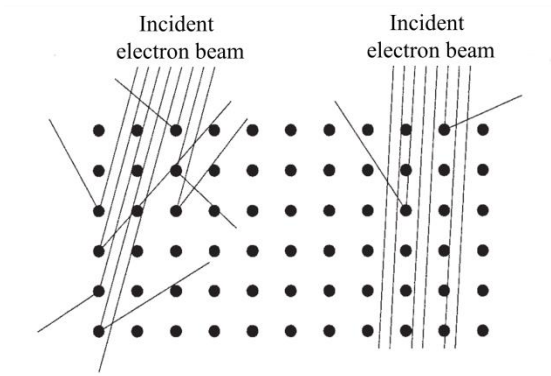

Figure 8 Schematic drawing of the variation in backscattered electron emission as a function of the relative orientation between the incident electron beam and the crystal lattice [75].

A Zeiss Ultra 55 field emission gun scanning electron microscope (FEG-SEM) was used to check the surface morphology of specimens as well as some fracture surfaces. All the microstructural investigations were performed in a Hitachi FEG-SEM SU-70 by using the ECCI technique. Cross-sections of selected specimens after corrosion test from both longitudinal and transversal directions were also examined.

6.4.4. X-ray diffraction

A number of techniques are available for measuring residual stresses. Some are destructive, while others are nondestructive; some have good spatial resolution, whereas others are restricted to near surface stresses. In the current work, laboratory X-ray diffraction (XRD) was chosen for the residual stress measurements.

To make a stress measurement by X-ray diffraction, the orthogonal coordinate systems should be introduced. As shown in Figure 9, the axes S_i define the specimen coordinate system with S_1 and S_2 in the specimen surface. The laboratory coordinate system L_i (connected with the direction of measurement) is defined so that L_3 is in the normal direction to the family of planes (hkl) [76]. The residual stress measurement by XRD is based on the measurement of variations of the inter-planer spacing (Δd) of a family of crystallographic planes versus their orientation (ψ) with regard to the surface of the specimen.

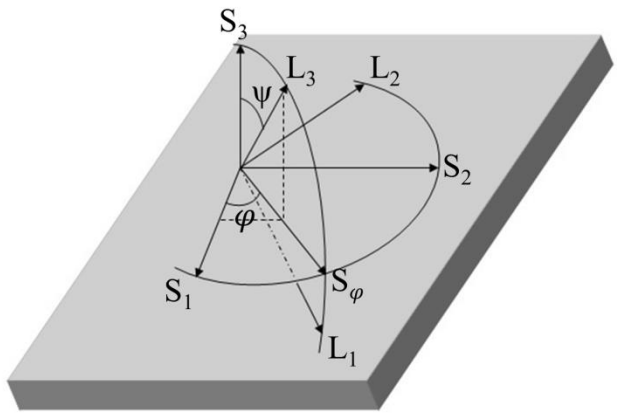

Figure 9 Schematic illustration of the orthogonal coordinate systems used in residual stress measurement by X-ray diffraction method [76].

Elastic strain $\varepsilon_{\varphi\psi}$ is determined by the variations of the inter-planer spacing, which is related to the displacement of the diffraction peak (Bragg angle θ):

$$\varepsilon_{\varphi\psi} = \frac{d_{\varphi\psi} - d_0}{d_0} = \frac{\Delta d}{d_0} = -\cot\theta \cdot \Delta\theta \qquad 6.1$$

Where d_0 is the stress free lattice spacing of the measured plane.

This strain can be expressed in terms of ε_{ij} in the specimen coordinate system [27]:

$$\varepsilon_{\varphi\psi} = \varepsilon_{11}\cos^2\varphi\sin^2\psi + \varepsilon_{12}\sin2\varphi\sin^2\psi + \varepsilon_{22}\sin^2\varphi\sin^2\psi + \varepsilon_{33}\cos^2\psi$$
$$+\varepsilon_{13}\cos\varphi\sin2\psi + \varepsilon_{23}\sin\varphi\sin2\psi \qquad 6.2$$

By Hook's law for isotropic material:

$$\varepsilon_{ij} = \frac{1+v}{E}\sigma_{ij} - \delta_{ij}\frac{v}{E}(\sigma_{11} + \sigma_{22} + \sigma_{33}) \qquad 6.3$$

Where δ_{ij} is Kronecker's delta, which equals to 1 when $i = j$ and 0 when $i \neq j$; E and v are Young's modulus of elasticity and Poisson's ratio, respectively.

Combining all the three equations above, thus:

$$\frac{d_{\varphi\psi} - d_0}{d_0} = \frac{1+v}{E}(\sigma_{11}\cos^2\varphi + \sigma_{12}\sin2\varphi + \sigma_{22}\sin^2\varphi - \sigma_{33})\sin^2\psi$$
$$+\frac{1+v}{E}\sigma_{33} - \frac{v}{E}(\sigma_{11} + \sigma_{22} + \sigma_{33})$$
$$+\frac{1+v}{E}(\sigma_{13}\cos\varphi + \sigma_{23}\sin\varphi)\cdot\sin2\psi \qquad 6.4$$

In order to calculate the strains and stresses in the specimen, at least six independent measurements of inter-planer spacing $d_{\varphi\psi}$ in different directions are required, and in practice more points are measured to improve the accuracy.

If the stress tensor in the irradiated layer is biaxial ($\sigma_{33} = 0$, and shear components σ_{13}, $\sigma_{23} = 0$ as well), the '$\sin^2\psi$ method' [27] is commonly used. Equation 6.4 becomes

$$\frac{d_{\varphi\psi} - d_0}{d_0} = \frac{1+v}{E}\sigma_\varphi\sin^2\psi - \frac{v}{E}(\sigma_{11} + \sigma_{22}) \qquad 6.5$$

Where σ_φ is the in-plane stress component along the S_φ direction as shown in Figure 8 and given by

$$\sigma_\varphi = \sigma_{11}\cos^2\varphi + \sigma_{12}\sin 2\varphi + \sigma_{22}\sin^2\varphi \qquad 6.6$$

According to equation 6.5, a linear relationship of $d_{\varphi\psi}$ vs. $\sin^2\psi$ is predicted. The stress in the S_φ direction may be obtained from the slope of a least-squares line fitted to the data measured at various ψ, if the elastic constants E, v and the stress free plane spacing d_0 are known. In practice, it is difficult to obtain d_0 and therefore the lattice spacing measured at $\psi = 0°$ is often used for substitution. For a biaxial stress, the resulted error by this substitution is negligible.

For ground or machined surfaces, due to the presence of shear strains ε_{13} and ε_{23}, 'ψ-splitting', i.e. a non-linear $d_{\varphi\psi}$ vs. $\sin^2\psi$ plot is common. Under this circumstance, the Dölle-Hauk method [76] can be used. Equation 6.1 and 6.2 can be rewritten in the form

$$\frac{d_{\varphi\psi} - d_0}{d_0} = A + B\sin^2\psi + C\sin\psi\cos\psi \qquad 6.7$$

$$A = \varepsilon_{33}$$

$$B = \varepsilon_{11}\cos^2\varphi + \varepsilon_{22}\sin^2\varphi - \varepsilon_{33} + (\varepsilon_{12} + \varepsilon_{21})\sin\varphi\cos\varphi$$

$$C = (\varepsilon_{13} + \varepsilon_{31})\cos\varphi + (\varepsilon_{23} + \varepsilon_{32})\sin\varphi$$

The $d_{\varphi\psi}$ vs. $\sin^2\psi$ dependence have to be measured in plane by three azimuths $\varphi = 0°, 45°, 90°$. The strain tensors ε_{ii} and ε_{ij} can be determined from the $d_{\varphi\psi}$ vs. $\sin^2\psi$ measurements, and stress tensors σ_{ii} and σ_{ij} can be calculated using Hooke's law. For this method, the accurate value of the stress free plane spacing d_0 is necessary.

For the residual stress measurement in the current work, Cr-K_α radiation was used, giving diffraction peak at 2θ~128° for the {220} lattice planes of the austenitic phase and diffraction peak at 2θ~154° for the {211} lattice planes of the ferritic phase respectively. Diffraction peaks were measured at nine ψ-angles (ψ = ±55°, ±35°, ±25°, ±15°, 0°). The Pseud-

Voigt Profile [76] was used for peak fitting in order to determine the diffraction peak position and the Full Width at Half Maximum (FWHM), which is related to the plastic deformation of the material [77]. Residual stresses were calculated based on either the $\sin^2\psi$ method or the Dölle-Hauk method. The X-ray elastic constants, S_1 and $1/2S_2$, needed for the stress calculations are $-1.2\times10^{-6}MPa^{-1}$ and $6\times10^{-6}MPa^{-1}$ for austenitic {220} lattice planes and $-1.25\times10^{-6}MPa^{-1}$and $5.58\times10^{-6}MPa^{-1}$ for ferritic {211} respectively [78]. In-depth stress profiles were measured for some selected specimens by using controlled electrolytic polishing to remove material; no correction was made for the possible stress relaxation due to material removal by polishing. In addition, in-situ measurements of surface stresses were also made on 304L specimens subjected to loading in the same four-point bend fixtures used for the stress corrosion cracking tests (Paper III). After each step of loading added, the specimens were kept one hour for stress relaxation, then the actual surface residual stresses parallel to the loading direction were measured. The loading was increased in steps to levels of 10, 200, 300 and 500 MPa, calculated according to ASTM G39 [64]. After the measurements, all specimens were kept in the holder at 500MPa loading and put in a furnace at 155℃ for 24h; then they were cooled to room temperature in the furnace over another period of 24h. Surface residual stresses were measured again to investigate the stress relaxation.

7. Results and discussion

This thesis addresses the interlinked themes of surface integrity (Paper I, Paper II) and stress corrosion properties (Paper III). A brief overview of the three papers is presented first, followed by detailed discussions of the two themes.

7.1. Summary of appended papers

7.1.1. Paper I

Surface integrity of 2304 duplex stainless steel after different grinding operations

Surface integrity of machined components has significant effect on their service performance. Paper I investigates the surface and subsurface changes of duplex stainless steel 2304 induced by grinding operations using different process parameters. Of the three varied grinding parameters, abrasive grit size, grinding force and grinding lubrication, the abrasive grit size was found to have the largest influence. Surface defects, a highly deformed surface layer and the generated tensile residual stresses along the grinding direction were found to be the main damages in the ground surface. Residual stresses were demonstrated to have different levels in the austenitic and ferritic phases.

7.1.2. Paper II

Surface characterization of austenitic stainless 304L after different grinding operations

Austenitic stainless steel 304L is widely used as structural material. Paper II studied the grinding processes with regard to the quality of the ground surfaces. The grinding parameters varied were abrasive grit size, machine power and grinding lubrication. The induced normal grinding force, grinding surface temperature and metal removal rate was measured and surface property changes investigated. The conclusion is that using smaller grit size abrasive or using grinding lubrication can improve surface finish and deformation; surface deformation increased when increasing the machine power but this also decreased surface defects.

Moreover, the metal removal rate was significantly enhanced by using grinding lubrication.

7.1.3. Paper III

Effect of surface grinding on chloride induced SCC of 304L

Paper III characterized the stress corrosion cracking (SCC) susceptibility of ground 304L austenitic stainless steels in boiling magnesium chloride and investigated the role of residual stresses induced by grinding operations on the corrosion behaviour. In-situ measurements of surface stresses external four point bending were performed to evaluate the difference between the actual stress and the calculated loading according to ASTM G39. The results showed micro-cracks initiated in the surface as a result of high tensile residual stresses originated from the grinding operations. Due to the anisotropy of residual stress induced by grinding, susceptibility to Cl-SCC was increased by grinding along the loading direction while grinding perpendicular to the loading direction improved SCC resistance. After cracks initiated, relief of surface tensile residual stresses has been observed; this is likely to arrest microscopic cracks and inhibit initiation of further cracks.

7.2. Influence of grinding on surface integrity

Surface integrity, expressed in terms of surface roughness, surface defects, near surface microstructural alterations and residual stresses after surface grinding, has been studied for both austenitic stainless steel 304L (Paper II, Paper III) and duplex stainless steel (Paper I). For both materials, the influence of grinding parameters including abrasive grit size (Group i), machine power (Group ii) and grinding lubricant (Group iii) has been investigated.

7.2.1. Surface roughness

Surface roughness resulting from different grinding parameters was measured through both Ra and Rz factors which are compared in Table 4; the trends showed similarity for both 304L (Paper I) and 2304 (Paper II). From the measured results, most significant parameters are identified as abrasive grit size (Group i) and grinding lubricant (Group iii). The highest surface roughness was induced by using coarse grit size (60#) abrasives, giving an Ra value of 1.81μm with an Rz value of 18.4μm for 304L and an

Ra value of 1.45μm with an Rz value of 15.84μm for 2304. Much smoother surfaces were obtained by using finer grit size abrasives as the final surface finish or grinding lubricant during the operations. By using the finest grit size (400#) abrasives, Ra and Rz values decreased dramatically; Ra=0.34μm, Rz=5.66μm were measured for 304L and Ra=0. 4μm, Rz=6.4μm for 2304. It is interesting to note that the two materials show slightly different responses with the two abrasive grit sizes: the austenitic steel has a slightly higher roughness than the duplex with 60# abrasive while the reverse is seen with 400# abrasive. Applying the statistical Student's t test indicates that the difference between results for 304L and 2304 with same grinding is significant at the 95% confidence level. By using grinding lubricant, both Ra and Rz values decreased to nearly half. On the other hand, machine power (Group ii) has very little influence on ground surface roughness; both Ra and Rz values changed very little although machine power has been doubled or tripled.

Table 4 Surface roughness from different grinding conditions for 304L austenitic stainless steel and 2304 duplex stainless steel, average and standard deviation for five measurements (n=5).

Group No.	Comparision		R_a (μm)		R_z (μm)	
			304L	2304	304L	2304
i	Abrasive grit size	60#	1.84±0.14	1.45±0.08	18.40±1.52	15.84±2.48
		180#	0.77±0.03	0.65±0.01	10.66±1.85	9.48±2.07
		400#	0.34±0.02	0.40±0.02	5.66±0.49	6.40±0.51
ii	Machine power	30%	0.79±0.09	0.76±0.03	8.56±0.61	10.48±1.08
		60%	0.77±0.03	0.65±0.01	10.66±1.85	9.48±2.07
		90%	0.75±0.05	0.69±0.01	9.11±2.38	7.94±0.63
iii	Lubrication	with	0.77±0.03	0.65±0.01	10.66±1.85	9.48±2.07
		without	0.38±0.05	0.41±0.01	7.11±0.16	5.13±0.4

7.2.2. Surface topography and surface defects

Similar surface defects have been observed after grinding operations for both austenitic stainless steel 304L (Paper II, Paper III) and duplex stainless steel 2304 (Paper I). As illustrated in Figure 10, deep grooving,

smearing, adhesive chips and indentations are the four types of defects found on the ground surfaces. The ground surface finish was influenced by the complex interactions between the abrasive grits and the workpiece surface. Deep grooving came from the uneven metal removal process, including chip forming and ploughing. Material around abrasive grit particles was pushed out and moved across the surface, which led to the formation of smearing areas. The redeposition process [22] introduced adhesive chips; the chips were transferred to the abrasive grit particles by adhesion, and then were transferred back to the ground surface by friction welding. Abrasive particles broke down into small pieces during grinding; because of the rubbing contact between these broke down particles or formed chips and the workpiece surface, indentations were formed on the ground surfaces.

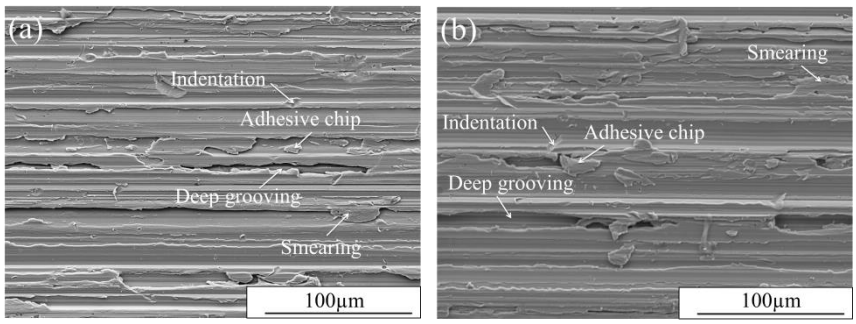

Figure 10 Surface topography and surface defects after grinding by 60# grit size abrasive, 60% machine power and without lubricant: (a) austenitic stainless steel 304L, (b) duplex stainless steel 2304.

The abrasive grit size (Group i) and grinding lubricant (Group iii) showed similar effects on the surface finish for 304L and 2304. The surface finish was clearly improved by using finer grit size abrasives or grinding lubricant; the reduction of surface defects was obvious. Smaller size of abrasive grits with a more even distribution and the largely reduced friction by lubricant are proposed to be the main factors respectively. On the other hand, the influence of machine power (Group ii) appeared to be different for these two materials. For duplex 2304, grinding with the intermediate machine power (60%) resulted in a better surface finish than grinding with lower (30%) or higher (90%) machine power. A lower machine power means a lower normal grinding force, which decreased cutting and ploughing but increased rubbing; while a higher machine

power means a higher downward force, which increased wear and friction between the abrasive grit and the workpiece surface. As a result, both lower and higher machine power generated more smearing areas and adhesive chips. However, the effect of varied machine power also depends on the properties of the workpiece material. Clear improvement of ground surface finish by increasing machine power up to 90% was observed in 304L. Austenitic stainless steels have high toughness and high ductility, 304L has been characterized as gummy during machining [16]. Increased machine power led to higher degree of strain hardening of the surface, thus the gummy behaviour was reduced and the final surface finish was improved.

7.2.3. Cross-section microstructure

Selected backscattered electron microscopy images showing typical cross-section microstructures near the grinding surfaces of austenitic 304L and duplex 2304 stainless steels are presented in Figure 11 and Figure 12 respectively. For all the images, the grinding direction is perpendicular to the sample cross-section. As illustrated in Figure 11(a) and Figure 12(a), similar features were observed for ground samples of both materials: (1) Smearing or adhesive chips, (2) a heavily deformed surface layer, (3) a deformation-affected subsurface layer and (4) bulk material. Depending on the grinding parameters and workpiece material, smearing or adhesive chips of different size and amount with irresolvable microstructure were observed. For the 304L material, in addition to smearing or adhesive chips, a large amount of cold welded chips with microcracks was also found along the ground surfaces (Figure 11(b)). During grinding, a heavily deformed surface layer extending only a few micrometers were formed; this layer showed similar features for both materials and comprised fragmented grains and dislocation sub-cells (Figure 11(b) and Figure 12(b)) although the thickness varied considerably with different grinding conditions. Below the heavily deformed surface layer, a deformation-affected subsurface layer with varying thickness was generated. Different features were observed in this layer for austenitic 304L and duplex 2304. For 304L, the subsurface layer was characterized by densely populated slip bands of multiple orientations, and the slip bands became fewer and straighter with increasing the depth from the ground surface where the degree of plastic deformation decreased (Figure 11). In the case of 2304, slip bands of different orientations in the austenite phase and

deformation fringes in the ferritic phase were observed (Figure 12(b)) with the intensity of deformation decreasing with increasing depth from the ground surface; the different microstructures are due to the different dislocation slip systems of the two phase during deformation. For all the ground samples, the grinding affected deformation zone was much smaller than the abrasive grit particle sizes.

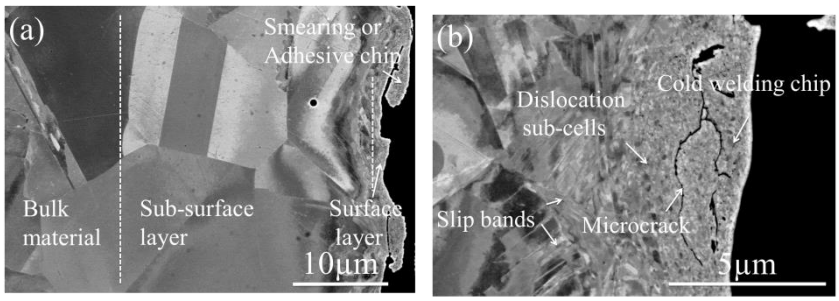

Figure 11 Cross-section microstructure of austenitic stainless steel 304L after grinding by different grit size abrasives (Group i): (a) 180#, (b) 60#.

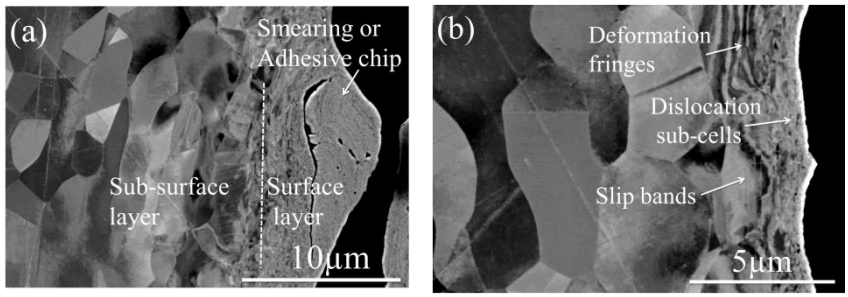

Figure 12 Cross-section microstructure of duplex stainless steel 2304 after grinding with different grit size abrasives (Group i): (a) 60#, (b) 400#.

From the cross-section investigations, the size and amount of ground surface defects (smearing, adhesive chips and or cold welded chips), as well as the thickness of deformed surface and subsurface layers, decreased appreciably when finer grit size abrasives (Group i) were used. This indicated an improved surface finish and smaller deformation; and the trend was similar for both 304L and 2304.

Compared with grinding at 60% machine power, both decreasing and increasing machine power led to a higher generation of defects along the ground surfaces (Group ii). A lower machine power (30%) means a lower

normal grinding force and less effective metal removal; so abrasive grit slides over the workpiece surface and can introduce many small smearing areas and adhesive chips. However, a lower grinding surface temperature also reduced cold welding chip formation on the ground 304L surfaces with lower machine power. A higher machine power (90%) increased friction and wear as well as the grinding surface temperature and as a result, more smearing areas and cold welded chips were formed. Machine power was found to have only a small influence on the deformation intensity and deformation depth for both materials, although deformation was found to be very uneven when using 30% machine power.

Using grinding lubricant (Group iii) largely reduced the formation of surface defects on the ground surfaces for both materials and the reduction in deformation depth is also obvious; this can be simply explained by the measured lower grinding surface temperature and lower normal grinding force. Using lubricant was also found to give more even deformation.

7.2.4. Residual stresses

Surface residual stresses for all the ground 304L samples (Paper II) and in-depth residual stresses of selected ground 2304 (Paper I) and 304L (Paper III) samples were measured. The origin of residual stress formation by grinding operation was described in section 3.2 in this thesis.

The measured in-depth residual stress profiles of as-delivered 304L austenitic stainless steel showed near-zero residual stresses from the surface to subsurface, while grinding operations generated surface tensile residual stresses parallel ($\sigma_{\parallel}$) and compressive residual stresses perpendicular ($\sigma_{\perp}$) to the rolling/grinding directions. The observed large degree of surface residual stress anisotropy as well as the measured relative low grinding surface temperatures indicated anisotropy mechanically induced residual stresses dominate over isotropy thermal effect in the current work. The coarse grit size (60#) abrasive gave rise to the highest surface tensile residual stress, up to 361±46MPa. However, the surface tensile stress dropped rapidly and became a compressive stress at a depth of around 15μm. The measured compressive $\sigma_{\perp}$ was

relative low in the surface layer, but increased rapidly in the subsurface and reached a peak of almost 250MPa. Measured surface residual stresses by different grinding conditions are presented in Table 5. Due to the lower surface deformation, i.e. lower mechanical effect, the surface tensile stress was reduced by using finer grit size (180#) or abrasive (Group ii). Compared with 180#, the use of even finer grit size (400#) abrasive induced more tensile residual stresses in both directions, which is probably due to the increased thermal effect in that more heat is generated by the subsequent grinding steps, in combination with the decreased mechanical effect. A higher machine power generated higher tensile $\sigma_{\parallel}$ but lower compressive $\sigma_{\perp}$; the increased thermal effect was considered as the main factor. The use of grinding lubricant decreased both mechanical and thermal effects. The measured results showed both surface tensile and compressive stresses were reduced (Group iii), which indicated the reduction of mechanical effect was more significant.

Table 5 Surface residual stresses induced by different grinding conditions of 304L austenitic stainless steel.

Group No.	Comparision		Surface residual stress (MPa)	
			$\sigma_{\parallel}$	$\sigma_{\perp}$
i	Abrasive grit size	60#	361±46	-91.1±18
		180#	228±25	-91.4±15
		400#	278.6±33	-22.4±10
ii	Machine power	30%	158.4±36	-142±20
		60%	228±25	-91.4±15
		90%	268.8±26	-54.5±13
iii	Lubrication	with	228±25	-91.4±15
		without	198.5±20	-35.8±14

Compared with the austenitic 304L, residual stresses in duplex 2304, which contain two phases, are more complicated. The measured and calculated results are presented as phase stresses, macro-stress and micro-stress in the current work. Phase stresses are residual stresses measured in the austenitic phase (FCC, σ^{γ}) and ferritic phase (BCC, σ^{α}). Macro-stresses (σ^{M}) are homogeneous residual stresses on a macroscopic scale along at least one direction [27]. Micro-stresses here are referred to the stresses balanced between the austenite ($\sigma^{m,\gamma}$) and ferrite ($\sigma^{m,\alpha}$); they are stresses on a microscopic scale [27]. The macro and micro stresses are calculated according to the following equations [76]

$$\sigma^{M} = V^{\gamma}\sigma^{\gamma} + (1 - V^{\gamma})\sigma^{\alpha} \quad 7.1$$

$$\sigma^{m,\gamma} = \sigma^{\gamma} - \sigma^{M} \quad 7.2$$

$$\sigma^{m,\alpha} = \sigma^{\alpha} - \sigma^{M} \quad 7.3$$

where V^{γ} is the volume fraction of the austenitic phase.

The abrasive grit size effect on the in-depth residual stress profiles parallel ($\sigma_{\parallel}$) and perpendicular ($\sigma_{\perp}$) to the rolling/grinding direction for 2304 is illustrated in Figure 13 for grinding using 60# and 180# grit size abrasive. The residual stress profiles exhibited similar trends for these two grinding conditions. As shown in Figure 13(a) and (b), different residual stresses were induced between the austenitic and the ferritic phases. In the austenitic phase (Figure 13(a)), tensile $\sigma_{\parallel}$ was observed in a surface layer of about 10μm with the highest (over 300MPa for the 60# abrasive) in the surface while compressive $\sigma_{\perp}$ was found in a thicker layer with a low value in the surface and a peak value (almost 300MPa for the 60# abrasive) in the subsurface region. In the ferritic phase (Figure 13(b)), except for the surface $\sigma_{\parallel}$ for grinding with 60# abrasives, both $\sigma_{\parallel}$ and $\sigma_{\perp}$ are compressive with a subsurface peak value and $\sigma_{\perp}$ is more compressive than the $\sigma_{\parallel}$. On the macroscopic scale (Figure 13(c)), $\sigma_{\parallel}$ exhibited a thin layer of tensile residual stresses followed by a thicker layer of compressive stresses, while $\sigma_{\perp}$ remained compressive in the stressed zone. The microscopic residual stresses (Figure 13(d)) revealed that the induced tensile residual stresses in the austenitic phase are balanced by the compressive residual stresses in the ferritic phase in both directions. In

both phases, the residual stresses reduced gradually from surface to subsurface regions, becoming nearly zero in the bulk material. For all the residual stress results shown in Figure 13, higher residual stresses in both surface and subsurface with greater penetration depth were generated by grinding using 60# grit size abrasive than 180#; this can be explained by the higher deformation and greater deformation depth using coarser abrasive grits.

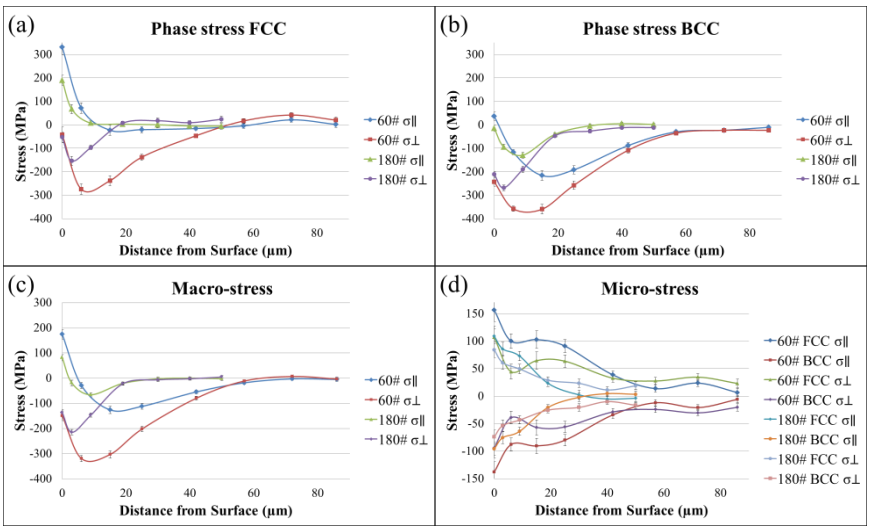

Figure 13 In-depth residual stresses of 2304 after grinding using different grit size abrasives (Group i): (a) residual stresses in austenitic phase, (b) residual stresses in ferritic phase, (c) macro-stresses, (d) micro-stresses. Positive values denote tensile stresses and negative compressive stresses.

The trends of the residual stress profiles were similar when grinding using different machine power or grinding lubricant (Paper II). Compared with grinding using 60% machine power (Group ii), a higher machine power (90%) introduced more tensile phase and macro residual stresses in both directions; a logical explanation is that higher machine power induced higher normal grinding force, which increased friction between the abrasive grit and the workpiece surface, thus more heat was generated. However, machine power was found to have little effect on the microscopic stresses and the penetration depth. Grinding using lubricant (Group iii) shifted $\sigma_{\parallel}$ towards more tensile and largely reduced $\sigma_{\perp}$ with lower compressive values in both macro and phase stresses. On the

microscopic scale, the absence of lubricant led to higher micro-stresses in both austenitic and ferritic phases and in both directions. The grinding lubricant reduced the grinding temperature, so surface stresses would be expected to be shifted towards compressive; however, the opposite was observed. The introduction of lubricant not only changed surface temperature, but also surface topography and deformation depth, all of which will affect the final stress field; the observed results indicated that the reduction of mechanical effects is more significant than that of temperature in the current work.

The FWHM (full width at half maximum) reveals broadening of the diffraction peak, which is related to the accumulation of plastic deformation [77]. For 304L, a lower FWHM in the ground surface layer was measured when using finer grit size abrasive or grinding lubricant, indicating smaller surface deformation; while the influence of machine power is relatively small. In the case of 2304, in-depth FWHM was observed to decrease with increasing depth from the ground surface in both austenitic and ferritic phases, which is illustrated in Figure 14 for grinding using 60# and 180# grit size abrasives. The trend indicated a gradient of plastic deformation under the surface. The FWHM results with varying abrasive grit size (Group i) showed higher deformation intensity and bigger deformation depth by grinding using coarser (60#) grits compared to 180#. The influence of machine power (Group ii) on surface and subsurface deformation is similar and dry grinding (Group iii) caused slightly higher deformation. All the FWHM results for both materials agree with the observed cross-section microstructure changes by different grinding operations.

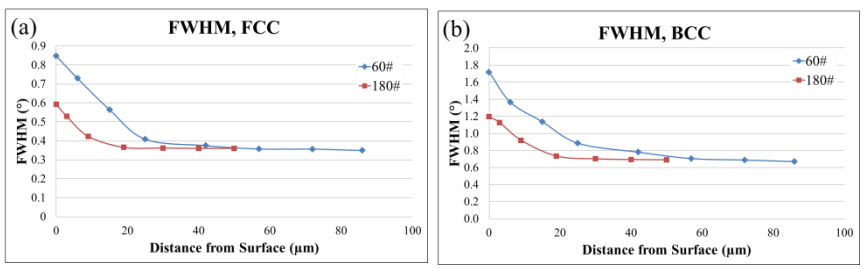

Figure 14 Full width at half maximum of 2304 by using different grit size abrasives (Group i): (a) austenitic phase, (b) ferritic phase.

7.3. Influence of grinding on chloride induced SCC

7.3.1. Corrosion behaviour without external loading

No macro-cracks occurred during exposure in the absence of external loading for either ground or as-delivered specimens. In the current work, macro-cracks are defined as those that can be observed by stereo microscopy with highest magnification of ×63. However, extensive stress corrosion micro-cracks were observed on all the ground surfaces. Typical SEM images showing surface morphology after exposure are presented in Figure 15. As shown in Figure 15(a), the micro-cracks tended to initiate perpendicular to the grinding direction with branching at angles to the initial micro-cracks. In the case of as-delivered material (Figure 15(b)), there is no evidence of such cracking; the slightly etched grain boundaries were due to the pickling process, which is typical for a 2B surface. A few small pits were also observed on all specimen surfaces.

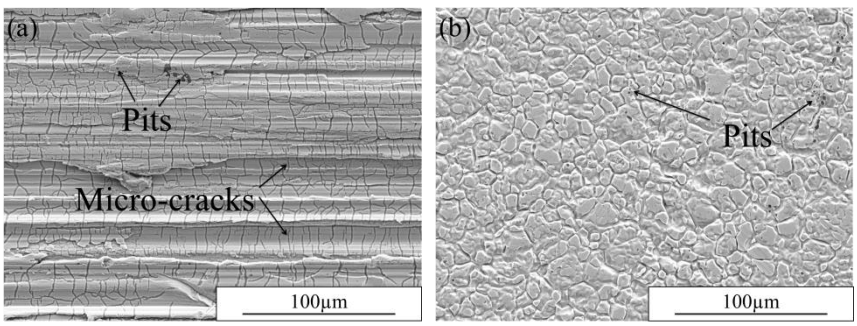

Figure 15 Surface morphology after exposure without external loading: (a) ground-RD specimen, (b) as-delivered specimen.

As illustrated in Figure 16, which are ECC images of the cross-section microstructures, micro-cracks in absence of external loading appeared mainly perpendicular to the grinding direction (Figure 16(a)); while along the grinding marks (Figure 16(b)), only small points of attack, which had not developed into cracks, were seen. The results agree well with the surface morphology investigations. High levels of surface tensile residual stress, up to 350MPa, were measured parallel to the grinding direction and surface compression in the perpendicular direction. The results strongly indicated that surface residual tensile stresses made 304L austenitic stainless steel prone to Cl-SCC even without external loading

while the compressive stresses retarded crack initiation. The observed micro-cracks initiated from the ground surface and ranged in depth from less than 1μm up to more than 10μm; they were largely within the highly deformed surface layer. This depth correlated to the shift from residual stresses from tensile to compressive under the ground surfaces. Both intergranular and transgranular micro-cracks were present.

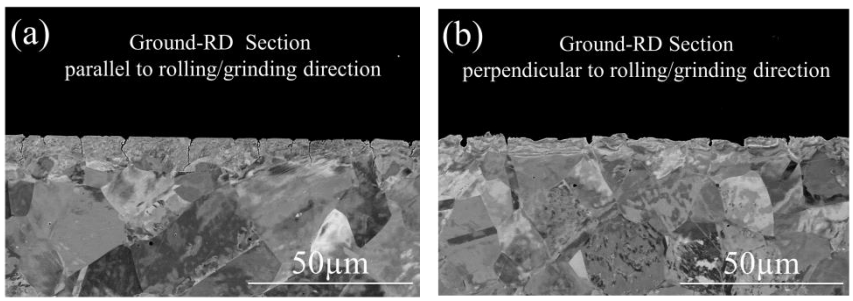

Figure 16 Cross-section microstructures after exposure without external loading: (a) ground-RD section parallel to rolling/grinding direction, (b) ground-RD section perpendicular to rolling/grinding direction.

7.3.2. In-situ measurement of surface stress

Surface stresses of ground and as-delivered specimens under the four point bending, which revealed the deviation between the actual surface stress and the values calculated according to ASTM G39 [64], are presented in Figure 17. For the as-delivered material, one extra specimen with one more step of loading (110MPa) was measured; the repeated results showed good accuracy and repeatability of the measurement. As shown in the figure, the results were strongly affected by the surface condition. For the as-delivered material, the actual surface stresses were close to the calculated values in the elastic regime. However, above the proof stress, which is around 230MPa for this material, the slope of the curve decreased dramatically; the actual stress decreased to nearly half of the calculated applied loading. This underlines very well the limitation expressed in ASTM G39 that the valid range for four-point bend loading is only up to the proof stress. On the other hand, due to the strain hardening in the surface layer from grinding operations, both curves of the ground specimens showed linear trend over the whole loading range. The slope of the ground-RD specimen was a little higher than that for the ground-TD specimen. For the ground-RD specimen, the measured

surface stress was a little lower than the sum of the tensile residual stress from grinding plus the calculated loading value, which may be due to the compressive residual stresses beneath the ground surface. In the case of ground-TD specimen, grinding generated surface compression in the loading direction (transverse to grinding/rolling direction) as well as more pronounced value in the subsurface, thus the measured surface stress became even lower than the sum of grinding induced compressive residual stress and the applied loading.

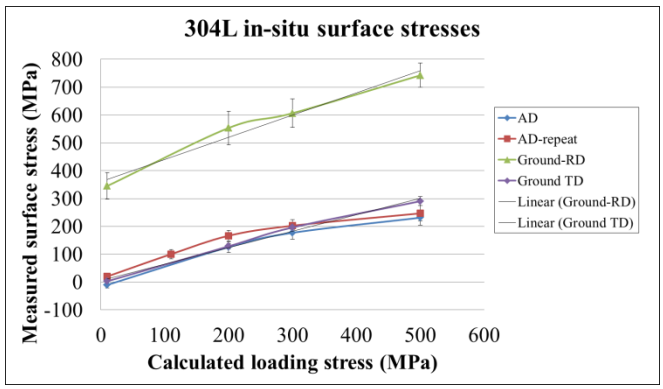

Figure 17 Measured surface stresses in the loading direction for four-point bending with different surface conditions of 304L austenitic stainless steel.

7.3.3. Corrosion behaviour with four-point bend loading

A summary of the macro-crack examination for the corrosion tests under four-point bend loading is tabulated in Table 6. One out of three as-delivered specimens was cracked through thickness after exposure with 50MPa loading. Increasing the loading up to 110, 200 or 300MPa caused all the as-delivered specimens to crack within 24h. Large cracks were observed on both ground-RD specimens with only 50MPa loading. However, no macro-cracks were seen at 50MPa or 110MPa applied loading for the ground-TD specimens. Compared with as-delivered specimens, the results clearly indicate that SCC susceptibility is increased by parallel grinding but decreased by transverse grinding, although micro-cracks initiated in both types of specimen surfaces. The SCC susceptibility also increased with increased loading, which can be simply explained by the role of grinding induced residual stresses combined with the applied stresses. From the measured or interpolated actual surface

stresses (Table 6), there seems to be a threshold stress of around 50MPa for the micro-cracks to occur for this material.

Table 6 Macro- and micro-crack examination after exposure with four-point bend loading; the measured or interpolated surface stresses from Figure 16 are also included for comparison.

Specimen	Applied four-point bend loading (MPa)	Measured (or interpolated) surface stress (MPa)	Exposure time	No. of specimens tested	No. of exposed specimens with macro-cracks	Micro-cracks
As-delivered	50	(20), (50)	24h	3	1	No
	110	100		2	2	No
	200	126, 166		2	2	No
	300	177, 202		2	2	No
Ground-RD	50	(400)		2	2	Yes
	300	607		2	2	Yes
Ground-TD	50	(35)		2	0	Yes
	110	(70)		2	0	Yes

Surface morphology investigations of all the exposed specimens showed macro-cracks to exhibit similar features. Multiple cracks with one major crack through the specimen usually appeared when cracking occurred. The cracks were perpendicular to the loading direction and tended to run parallel to each other. Example of surface morphologies after exposure with 50MPa four-point bend loading of the three types of specimens can be seen in Figure 18. The macro-cracks appeared to be wide and exhibited multiple branching (Figure 18(a), (c)). For the ground surfaces, micro-cracks with extensive branching were also observed without external loading and tended to be orientated perpendicular to the grinding direction. This applied even for the ground-TD specimens, indicating the residual stress effect outweighed the applied load effect and the possible micro-notch effect from the grinding marks within the experiment range investigated (applied load $\leq$ 110MPa). Varying degrees of pitting were

observed for all specimens. From Figure 18 (a) and (b), pits on the ground surfaces showed some tendency to follow the micro-cracks and connect together perpendicular to the grinding marks. Moreover, cracks were seen to extend from pits, indicating the pits may be precursors to cracks.

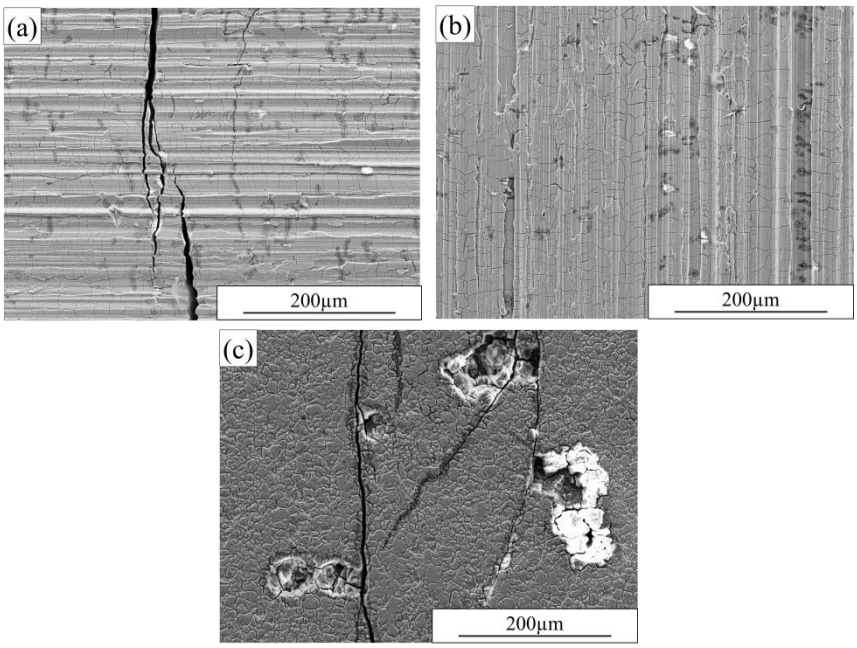

Figure 18 Surface morphology after exposure with 50MPa four-point bend loading: (a) ground-RD cracked specimen, (b) ground-TD uncracked specimen, (c) as-delivered cracked specimen.

Cross-sectional investigations showing stress corrosion cracking after exposure are illustrated in Figure 19 for cracked ground-RD and AD specimens under 50MPa four-point bend loading. The macro-crack path appeared mainly branched and transgranular. Pits were evident from the surface and all macro-cracks were associated with such pits. Micro-cracks were also seen to initiate from the ground surface, but they were not associated with pits and they were not observed in AD cross-section.

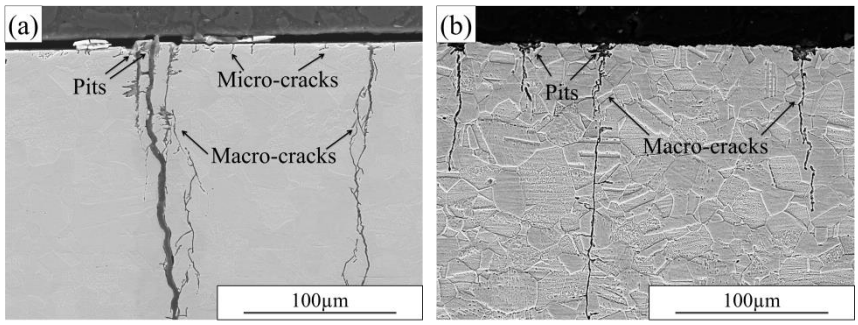

Figure 19 Cross-section microstructures after exposure with 50MPa four-point bend loading: (a) ground-RD specimen sectioned parallel to the rolling/grinding and loading direction, (b) as-delivered specimen sectioned parallel to the rolling and loading direction.

Detailed ECCI investigations of cross section showed pits and micro-cracks which agreed with the surface morphology study. For the ground-RD specimens, the penetration depth of micro-cracks was increased by the four-point bend loading, especially in the direction perpendicular to loading and grinding. In the case of ground-TD specimens, the loading significantly increased the penetration depth and density of micro-cracks in the direction perpendicular to loading, i.e. parallel to the rolling/grinding direction; but in the direction parallel to loading, the change was small. Figure 20 is a detailed characterization of micro-cracks and shows how multiple cracks could originate from a single pit. The micro-cracks initiated either parallel to or cross the deformation slip bands from the pit bottom. Both transgranular and intergranular micro-cracks were observed.

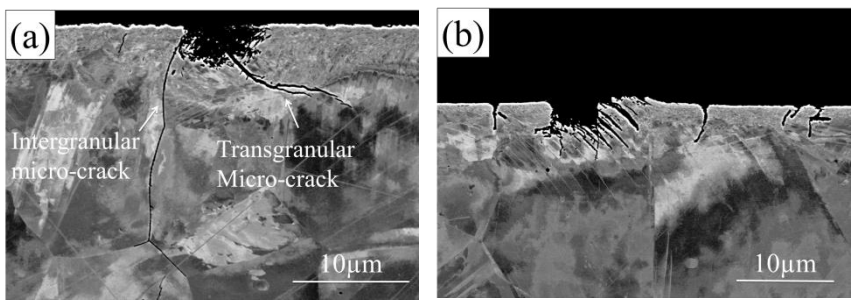

Figure 20 Cross-section microstructure after exposure with 50MPa four-point bend loading: (a) ground-RD sectioned parallel to rolling/grinding direction, (b) ground-TD sectioned parallel to rolling/grinding direction.

When pitting and stress corrosion cracking are observed together, there is always a question about whether pits formed from cracks, or cracks initiated from pits. In the current work, no macro-cracks were observed without an associated pit, but pits were found without evident macro-cracks, also multiple cracks were seen to originate from the pit bottom. It thus seems that pits act as precursors to cracking in this investigation, in agreement with some other studies [58] [19] [46]. Micro-cracks initiated only on the ground surfaces, indicating grinding-induced surface tensile stresses were the main driving force for micro-crack initiation. The surface morphology investigation showed pits tended to develop on the micro-cracks (Figure 18 (a) (b)). In the case of ground-RD specimens, these pits appeared to grow together along the micro-cracks in the direction perpendicular to the grinding marks and let to the initiation of macro-crack. Even in the ground-TD specimens where no macro-crack was found, pits initiated from the micro-cracks and tended to grow together in the dominant micro-cracking direction i.e. perpendicular to rolling/grinding direction, instead of the loading direction. All these results suggested that micro-cracks occurred first, followed by pitting initiation from these micro-cracks and then the development of macro-cracks. Investigated fracture surfaces of both ground-RD and AD specimens (Figure 21) showed typical cleavage fracture which is predominantly transgranular with some local indications of intergranular cracking. Moreover, some indications of crack branching are observed. The results agreed with the cross-section investigations.

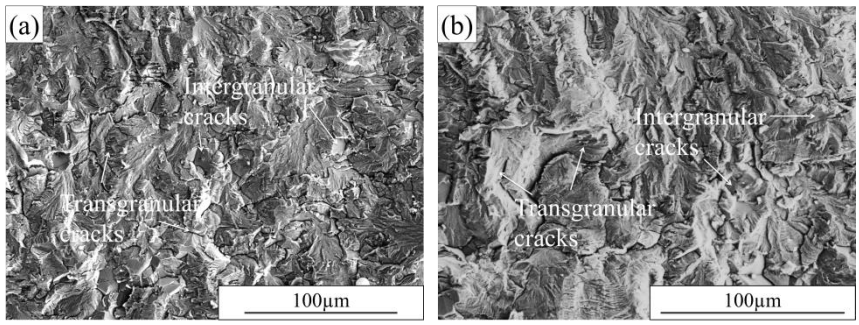

Figure 21 Fracture surfaces after exposure with 50MPa four-point bend load: (a) ground-RD specimen, (b) as-delivered specimen.

7.3.4. Stress relaxation after exposure

Surface stresses of ground specimens were measured both before and after exposure. As shown in Figure 22, surface grinding induced tensile residual stresses reduced dramatically from 350MPa to below 100MPa after exposure without external loading while surface compression increased slightly. This can be directly related to the micro-crack formation which relaxed surface tension. For the ground-RD specimens (Figure 22(a)), after exposure with 50MPa applied load, surface tensile stressed dropped to below 50MPa; while the corresponding figure for the 300MPa loading was zero. This is attributed to the formation of both micro- and macro-cracks. Surface stress relaxation was similar between exposure without and with applied load for the ground-TD specimens (Figure 22(b)); this specimen exhibited no macro-cracking so surface stress relaxation was caused by the micro-crack formation. Moreover, the measured low level of stress relaxation after heat treatment at 155℃ for 24 hours under 500MPa four-point bend loading, shown in Figure 23, indicated that the relaxation of tensile residual stresses after exposure are mainly due to the cracking of the specimens.

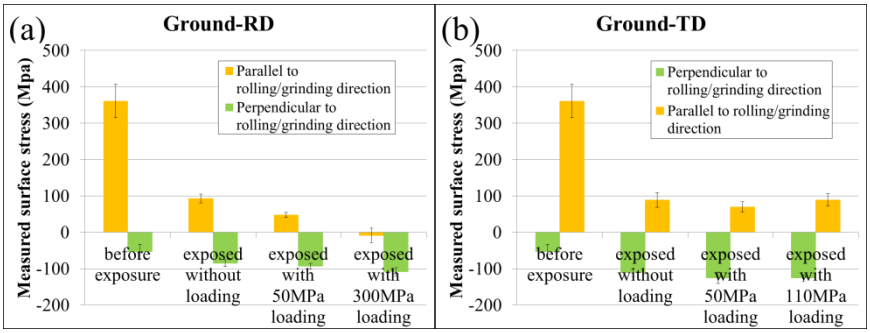

Figure 22 Surface residual stresses of ground specimens parallel and perpendicular to rolling/grinding directions before and after exposure: (a) ground-RD specimen, (b) ground-TD specimen.

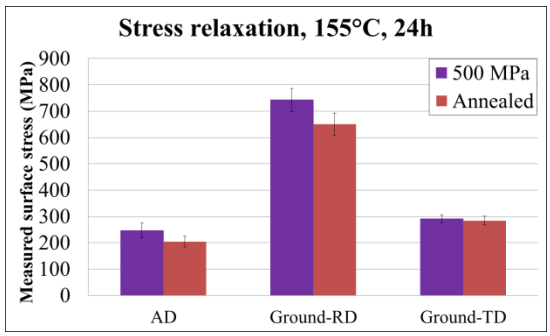

Figure 23 Stress relaxation of four-point bend specimens after heat treatment at 155℃ for 24h for AD and ground specimens.

In-depth residual stress profiles of a ground-specimen before and after exposure without external loading as well as the in-depth surface morphology after exposure are presented in Figure 24. Results showed that after exposure the tensile stress dropped from the surface to the subsurface until reaching a near-zero state where almost all the micro-cracks stopped. This indicates that micro-cracks initiated due to the high level of surface residual stresses; that their formation largely released the surface tensile stress and that they stopped when there was no longer an acting tensile stress. In-depth surface morphology showed penetration depths of micro-cracks are very uneven; some of them disappeared after surface polishing of 2μm in thickness, while some penetrated to a depth over 10μm. The results agreed with the cross-section observation.

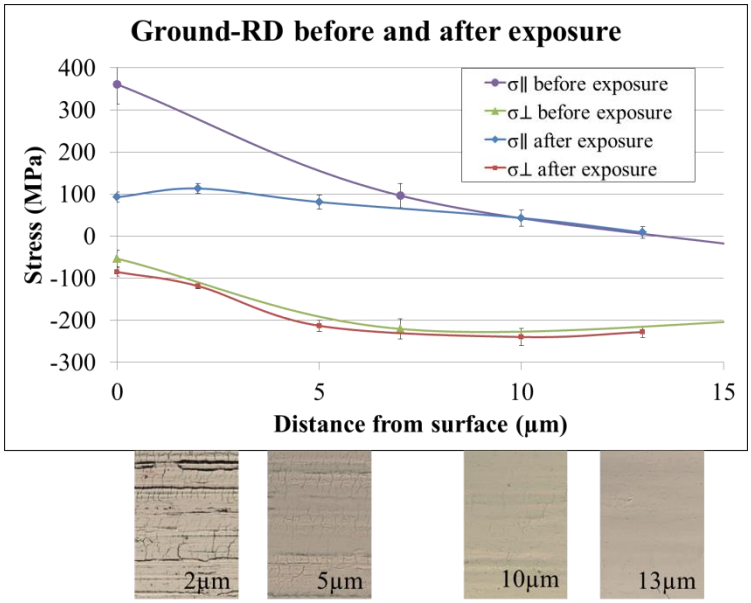

Figure 24 In-depth residual stress profiles in both parallel and perpendicular to rolling/grinding directions of ground-RD specimen before and after exposure without external loading as well as the in-depth surface morphology.

8. Conclusions

This work has addressed some aspects of the interplay between grinding operations, surface integrity and stress corrosion properties for stainless steels, following conclusions can be drawn:

- Surface roughness and surface defects can be largely decreased by using smaller grit size abrasives or by using grinding lubricant for both austenitic stainless steel 304L and duplex stainless steel 2304. The influence of machine power on surface roughness was small. Surface defects can be reduced by using a higher machine power for 304L; however, for 2304, there was an optimum value below or above which the surface defects became more pronounced.
- Microstructure investigations of both 304L and 2304 indicate that the cross-section of the ground stainless steel samples can be divided into four layers: a surface layer with smearing, adhesive chips or cold welded chip, a heavily deformed surface layer, a deformation affected subsurface layer and the bulk material. The thickness of each layer varied depending on the grinding parameters used.
- Grinding 304L or 2304 resulted in high level of tensile residual stresses along the grinding direction and compressive residual stresses perpendicular to the grinding direction in the surface layer. Beneath the ground surface, a subsurface layer of compressive residual stresses in both directions were formed. The residual stress level depended on the grinding condition. The pronounced anisotropy of the residual stresses in the current work indicated that mechanical effects dominated over thermal effects from heating of the workpiece, since the latter would be expected to be isotropic.
- For the duplex 2304, grinding generated different levels of residual stresses in the two phases with tensile micro-stresses in the austenitic and compressive micro-stresses in the ferritic phase.
- In-situ surface stress measurements of 304L under four-point bend loading demonstrated that the actual load may deviate from the calculated value using the formula according to ASTM G39; the

deviation depended on the surface conditions and the proof stress. The absolute value was strongly affected by the residual stresses in the surface and subsurface layers of the material.

- Extensive micro-cracks were observed to initiate on ground surfaces of 304L after exposure to boiling magnesium chloride and could be related to grinding-induced surface tensile residual stresses. The micro-cracks arrested in a region with low or no tensile residual stresses. Macroscopic cracking leading to final failure only occurred under an applied load, the role of residual stress in both surface and subsurface layers combined with the applied stress was suggest as the main factor, a threshold stress seems to be required for the macro-cracking to occur.
- In the present conditions it appeared that micro-cracks occurred first, followed by the pitting initiation from the micro-cracks. Pits acted as precursors and then originated macro-cracks, in which more pits will grow.
- The grinding direction with respect to the loading direction has been demonstrated to significantly affect the SCC susceptibility of 304L. Grinding along the loading direction caused the material to be highly prone to Cl-SCC, while grinding transverse to the loading direction improved the SCC resistance. The large degree of grinding induced residual stress anisotropy was suggested to be the main factor. It is proposed that grinding transverse to the main stress direction in a construction may be used to reduce the risk for cracking.

9. Further work

Based on the results obtained in this work, the following further work can be proposed:

1. Surface integrity of ferritic stainless steels after different grinding operations.

Comparison of the surface integrity of austenitic, duplex and ferritic stainless steels after similar grinding operations. Data for a ferritic steel would assist in understanding the surface changes as a result of grinding for the two phases of the duplex 2304 in this work.

2. Stress corrosion cracking behaviour of duplex and ferritic stainless steels after same grinding conditions as the current work for austenitic 304L (Paper III).

How does the duplex structure influence the SCC susceptibility after similar surface finishing processes? Can this help to explain the superior SCC resistance of duplex stainless steels compared to standard austenitic grades?

3. Stress corrosion cracking behaviour of austenitic or duplex stainless steels after different grinding operations.

To correlate different grinding parameters with surface integrity and corrosion properties.

10. References

[1] R. Pettersson and E. Johansson, "Stress corrosion resistance of duplex grades," in *Duplex stainless steel world conference*, Beaune, 2010.

[2] G. E. Dieter, Mechanical Metallurgy, McGraw Hill Higher Education , 1989.

[3] ISSF International stainless steel forum, "The stainless steel family".

[4] D. A. Jones, Principles and prevention of corrosion, Pearson Education (US) , 1996.

[5] C.-O. Olsson and D. Landolt, "Passive films on stainless steels - chemistry, structure and growth," *Electrochimica Acta,* vol. 48, no. 9, pp. 1093-1104, 2003.

[6] C.-O. Olsson, S. Malmgren, M. Gorgoi and K. Edström, "Quantifying the metal nickel enrichment on stainless steel," *Electrochemical and solid state letters,* vol. 14, pp. C1-C3, 2011.

[7] T. J. Mesquita, E. Chauveau, M. Mantel and R. P. Nogueira, "A XPS study of the Mo effect on passivation behaviors for highly controlled stainless steels in neutral and alkaline conditions," *Applied surface science,* vol. 270, pp. 90-97, 2013.

[8] J. Hawk, J. Simmons and J. Raviers, "Effect of nitrogen alloying on the microstructure and abrasive wear of stainless steels," *Journal of materials engineering and performance,* vol. 3, no. 2, pp. 259-272, 1994.

[9] D. Porter and K. Easterling, Phase transformations in metals and alloys, Chapman and Hall , 1992.

[10] Outokumpu, Corrosion Handbook, 2015.

[11] Outokumpu, Handbook of stainless steel, 2013.

[12] E. M. Trent and P. K. Wright, Metal cutting, BUTTERWORTH-HEINEMANN, 2000.

[13] J. Jurko, A. Panda and M. G. J. Behun, "Effect of machinability of stainless steels for increasing of productivity production," *Applied mechanics and materials,* vol. 378, pp. 154-158, 2013.

[14] J. Jurko, A. Panda, M. Behun and I. Mrkvica, "Prediction of selected aspects of machinability of austenitic stainless steels," *Advanced materials research,* vol. 739, pp. 206-209, 2013.

[15] E. Ezugwu, Z. Wang and A. Machado, "The machinability of nickel-base alloys: a review," *Journal of material processing technology,* vol. 86, pp. 1-16, 1998.

[16] D. Jang, T. Watkins, K. Kozaczek, C. Hubbard and O. Cavin, "Surface residual stresses in machined austenitic stainless steel," *Wear,* vol. 194, pp. 168-173, 1996.

[17] B. Leffler, S. Gunnarsson and M. Svensson, Maskinbearbetning av rostfria stål, Avesta Sheffield AB och författarna, 1995.

[18] H. Zhang, W. chen, X. Fu and L. Huang, "Temperature measurement and burn mechanism of stainless steel 1Cr11Ni2W2MoV in grinding," *Materials Science Forum,* vol. 723, pp. 433-438, 2012.

[19] A. Turnbull, K. Mingard, J. Lord, B. Roebuck, D. Tice, K. Mottershead, N. Fairweather and A. Bradbury, "Sensitivity of stress corrosion cracking of stainless steel to surface machining and grinding procedure," *Corrosion Science,* vol. 53, pp. 3398-3415, 2011.

[20] S. Acharyya, A. Khandelwal, V. Kain, A. Kumar and I. Samajdar, "Surface working of 304L stainless steel: Impact on microstructure, electrochemical behavior and SCC resistance," *Materials Characterization,* vol. 72, pp. 68-76, 2012.

[21] L. Jiang, J. Paro, H. Hänninen, V. Kauppinen and R. Oraskari, "Comparison of grindability of HIP austenitic 316L, duplex 2205 and Super duplex 2507 and as-cast 304 stainless steels using alumina wheels," *Journal of Materials Processing Technology,* vol. 62, pp. 1-9, 1996.

[22] D. Turley and E. Doyle, "Factors affecting workpiece deformation during grinding," *Material Science and Engineering,* vol. 21, pp. 261-271, 1975.

[23] J. Outwater and M. Shaw, "Surface temperature in grinding," *Trans.ASME,* vol. 74, pp. 73-86, 1952.

[24] C. Yao, Q. Jin, X. Huang, D. Wu, J. Ren and D. Zhang, "Research on surface integrity of grinding Inconel 718," *Int J Adv Manuf*

Technol, vol. 65, pp. 1019-1030, 2013.

[25] J. P. Davim, Surface integrity in machining, Springer London Ltd , 2010.

[26] M. Vashista, S. Kumar, A. Ghosh and S. Paul, "Surface integrity in grinding medium carbon steel with miniature electroplated monolayer cBN wheel," *JMEPEG,* vol. 19, pp. 1248-1255, 2010.

[27] I. Noyan and J. Cohen, Residual Stress Measurement by Diffraction and Interpretation, Springer-Verlag New York Inc. , 1987.

[28] G. Guo, Z. Liu, X. Cai, Q. An and M. Chen, "Investigation of surface integrity in conventional grinding of Ti-6Al-4V," *Advanced Materials Research,* Vols. 126-128, pp. 899-904, 2010.

[29] N. B. Fredj, H. Sidhom and C. Braham, "Ground surface improvement of the austenitic stainless steel AISI 304 using cryogenic cooling," *Surface & Coatings technology,* vol. 200, pp. 4846-4860, 2006.

[30] F. Brinksmeier, "The influence of process quantities in grinding on residual workpiece stresses," in *Conference on residual stresses*, Darmstadt, 1990.

[31] E. Rabinowicz and A. Mutis, "Effect of abrasive particles size on wear," *Wear,* vol. 8, pp. 381-390, 1965.

[32] M. Morre and P. Swanson, "The effect of abrasive particle shape on abrasive wear: a comparison of theory and experiment," in *Wear of Materials*, New York, 1983.

[33] G. Manimaran, M. Pradeep kumar and R. Venkatasamy, "Influence of cryogenic cooling on surface grinding of stainless steel 316," *Cryogenics,* vol. 59, pp. 76-83, 2014.

[34] I. Jawahir, E. Brinksmeier, R. Saoubi, D. Aspinwall, J. Outeiro, D.Meyer, D. Umbrello and A. Jayal, "Surface integrity in material removal processes: Recent advances," *CIRP annals - Manufacturing Technology,* vol. 60, pp. 603-626, 2011.

[35] M. Field and J. Kahles, "The surface integrity of machined and ground high strength steels," *DMIC Report,* pp. 210: 54-77, 1964.

[36] M. Field and J. Kahles, "Review of surface integrity of machined components," *Annals of the CIRP,* vol. 20, no. 2, pp. 153-162, 1971.

[37] M. Field, J. Kahles and J. Cammett, "Review of measuring methods

for surface integrity," *Annals of the CIRP,* vol. 21, pp. 219-238, 1972.

[38] ANSI, American National Standard on Surface Integrity, Society of Manufacturing Engineers, 1986.

[39] P. Kentish, "Stress corrosion cracking of gas pipelines - effect of surface roughness, orientations and flattening," *Corrosion Science,* vol. 49, pp. 2521-2533, 2007.

[40] S. Suresh, Fatigue of materials, Cambridge University Press , 1998.

[41] J.-P. Tinnes, C. Bosch, O. Raquet, G. Santarini and D. Delafosse, "Subcritical stress corrosion crack growth rate of a 316L austenitic stainless steel in boiling magnesium chloride," in *EDEN*, 2003.

[42] D. Novovic, R. Dewes, D. Aspinwall, W. Voice and P. Bowen, "The effect of machined topography and integrity on fatigure life," *International journal of machine tools and manufacture,* vol. 44, pp. 125-134, 2004.

[43] G. Krolczyk, S. Legutko and M. Gajek, "Predicting the surface roughness in the dry machining of duplex stainless steel (DSS)," *Metalurgija,* vol. 52, pp. 259-262, 2013.

[44] A. Khan, S. Abdulkareem and Z. Zain, "Effect of machining parameters on surface roughness during wet and drywire-EDM of stainless steel," *Journal of applied sciences,* vol. 11, pp. 1867-1871, 2011.

[45] P. Junlabuddee and C. Saikaew, "A study of factor attecting surface roughness in turning process of AISI 316L stainless steel by Shainin design of experiment method," *KKU engineering journal,* vol. 42, pp. 71-81, 2015.

[46] G. Hinds, L. Wickström, K. Mingard and A. Turnbull, "Impact of surface condition on sulphide stress corrosion cracking of 316L stainless steel," *Corrosion Science,* vol. 71, pp. 43-52, 2013.

[47] W. Li, T. Sakai, M. Wakita and S. Mimura, "Influence of microstructure and surface defect on very high cycle fatigue properties of clean spring steel," *International journal of fatigue,* vol. 60, pp. 48-56, 2014.

[48] M. Lei, X. Zhu and D. Guo, "Reducing geometrical, physical and chemical constraints in surface integrity of high performance stainless steel components by surface modification," *Jounal of*

manufacturing science and engineering, accepted to publish 2015.

[49] S. Ghosh and V. Kain, "Microstructural changes in AISI 304L stainless steel due to surface machinin: effect on its susceptibility to chloride stress corrosion cracking," *Journal of Nuclear Materials,* vol. 403, pp. 62-67, 2010.

[50] J. Du, Z. Liu and S. Lv, "Deformation-phase transformation coupling mechanism of white layer formation in high speed machining of FGH95 Ni-based superalloy," *Applied surface science,* vol. 292, pp. 197-203, 2014.

[51] Z. Chen, R. L. Peng, P. Avdovic, J. Zhou, J. Moverare, F. Karlsson and S. Johansson, "Effect of thermal exposure on microstructure and nano-hardness of broached Inconel 718," in *MATEC Web of Conferences*, Giens, France, 2014.

[52] C. Che-Haron and A. Jawaid, "The effect of machining on surface integrity of titanium alloy Ti-6% Al-4% V," *Journal of material processing technology,* vol. 166, no. 2, pp. 188-192, 2005.

[53] J. Lu, K. Luo, X. Cheng, J. Hu, F. Dai, H. Qi, L. Zhang, J. Zhong, Q. Wang and Y. Zhang, "Effects of laser peening on stress corrosion cracking (SCC) of ANSI 304 austenitic stainless steel," *Corrosion Science,* vol. 60, pp. 145-152, 2012.

[54] B. Zhang, W. Shen, Y. Liu, X. Tang and Y. Wang, "Microstructure of surface white layer and internal white adiabatic shear band," *Wear,* vol. 211, no. 2, pp. 164-168, 1997.

[55] P. Withers and H. Bhadeshia, "Residual stress Part 2 - nature and origin," *Materials science and thecnology,* vol. 17, pp. 366-375, 2001.

[56] K.-S. Lee, J.-K. Lee, K.-O. Song and J.-H. Park, "Study on effect of mechanical machining and heat treatment on surface residual stress of TP316L stainless steel," *Transactions of the Korean society of mechanical engineers,* vol. 35, pp. 453-458, 2011.

[57] Q. Feng, C. Jiang, Z. Xu, L. Xie and V. Ji, "Effect of shot peening on the residual stress and microstructure of duplex stainless steel," *Surface & coatings technology,* vol. 226, pp. 140-144, 2013.

[58] K. Lyon, T. Marrow and S. Lyon, "Influence of milling on the development of stress corrosion cracks in austenitic stainless steel," *Journal of Materials Processing Technology,* vol. 218, pp. 32-37,

2015.

[59] S. Shang, "Prediction of dimensional instability resulting from layer removal of an internally stressed orthotropic composite cylinder," *KSME international journal,* vol. 16, pp. 757-761, 2002.

[60] P. Marcus, Corrosion mechanisms in theory and practice, CRC Press Inc , 2012.

[61] E. Johansson and T. Prosek, "Stress corrosion cracking properties of UNS S32101- a new duplex stainless steel with low nickel content," in *Corrosin 2007 Conference & Expo*, 2007.

[62] ASTM, G36-94, Standard practice for evaluating stress-corrosion-cracking resistance of metals aned alloys in a boiling magnesium chloride solution, reapproved 2006.

[63] ASTM, G123-00, Standard test method for evaluating stress-corrosion cracking of stainless alloys with different nickel content in boiling acidified sodium chloride solution, reapproved 2011.

[64] ASTM, G39-99, Standard practice for preparation and use of bent-beam stress-corrosion test specimens, 2011.

[65] ASTM, G30-97, Standard practice for making and using U-bend stress-corrosion test specimens, Reapproved 2009.

[66] ASTM, G38-01, Standard practice for making and using C-ring stress-corrosion test specimens, 2013.

[67] ASTM, G129-00, Standard practice for slow strain rate testing to evaluate the susceptibility of metallic materials to environmentally assisted cracking, 2013.

[68] U. Kivisäkk and G. Chai, "Influence of test method and relaxation on the result from stress corrosion cracking tests of stainless steels in dilute neutral chlorides," *Corrosion,* vol. 59, pp. 828-835, 2003.

[69] Wikipedia, "Stereo microscope," [Online]. Available: https://en.wikipedia.org/wiki/Stereo_microscope.

[70] S. Reed, Electron microprobe analysis and scanning electron microscopy in geology, Cambridge University Press , 2010.

[71] J. I. Goldstein, D. E. Newbury, D. C. Joy, C. E. Lyman, P. Echlin, E. Lifshin, L. Sawyer and J. R. Michael, Scanning electron microscopy and X-Ray microanalysis, Kluwer Academic/Plenum Publishers , 2007.

[72] D. Coates, "Kikuchi-like reflection patterns obtained with the scanning electron microscope," *Philosophical magazine,* vol. 16, pp. 1179-1184, 1967.

[73] G. Booker, A. Shaw, M. Whelan and P. Hirsch, "Some comments on the interpretation of the 'kikuchi-like reflection patterns' observed by scanning electron microscopy," *Philosophical magazine,* vol. 16, pp. 1185-1191, 1967.

[74] S. Johansson, J. Moverare and R. Peng, "Recent applications of scanning electron microscopy," *Pract.Metallogr.,* vol. 50, pp. 810-820, 2013.

[75] D. C. Joy, D. E. Newbury and D. L. Davidson, "Electron channeling patterns in the scanning electron microscope," *Journal of applied physics,* vol. 53, pp. R81-R122, 1982.

[76] V. Hauk, Structural and Residual Stress Analysis by Nondestructive Methods, Elsevier Science Ltd , 1997.

[77] Z. Chen, R. Peng, P. Avdovic, J. Moverare, F. Karlsson, J. Zhou and S. Johansson, "Analysis of thermal effect on residual stresses of broached Inconel 718," *Advanced Materials Research,* vol. 996, pp. 574-579, 2014.

[78] B. Eigenmann and E. Macherauch, "Röntgenographische Untersuchung von Spannungszuständen in Werkstoffen Teil I und II und III," *Mat.-wiss. und Werkstofftech.,* no. 26, pp. 148-160 and 199-216, 1995.